

# SNR-calibrated Type Ia supernova models

Eduardo Bravo,<sup>1</sup><sup>★</sup> Carles Badenes,<sup>2,3</sup> Héctor Martínez-Rodríguez,<sup>2</sup>

<sup>1</sup>*E.T.S. Arquitectura del Vallès, Universitat Politècnica de Catalunya, Carrer Pere Serra 1-15, 08173 Sant Cugat del Vallès, Spain*

<sup>2</sup>*Department of Physics and Astronomy and Pittsburgh Particle Physics, Astrophysics and Cosmology Center (PITT PACC), University of Pittsburgh, 3941 O'Hara Street, Pittsburgh, PA 15260, USA*

<sup>3</sup>*Institut de Ciències del Cosmos (ICCUB), Universitat de Barcelona (IEEC-UB), Martí Franquès 1, E08028 Barcelona, Spain*

Accepted XXX. Received YYY; in original form ZZZ

## ABSTRACT

Current Type Ia supernova (SN Ia) models can reproduce most visible+IR+UV observations. In the X-ray band, the determination of elemental abundance ratios in supernova remnants (SNRs) through their spectra has reached enough precision to constrain SN Ia models. Martínez-Rodríguez et al have shown that the Ca/S mass ratio in SNRs cannot be reproduced with the standard nuclear reaction rates for a wide variety of SN Ia models, and suggested that the  $^{12}\text{C}+^{16}\text{O}$  reaction rate could be overestimated by a factor as high as ten. We show that the same Ca/S ratio can be obtained by simultaneously varying the rates of the reactions  $^{12}\text{C}+^{16}\text{O}$ ,  $^{12}\text{C}+^{12}\text{C}$ ,  $^{16}\text{O}+^{16}\text{O}$ , and  $^{16}\text{O}(\gamma, \alpha)^{12}\text{C}$  within the reported uncertainties. We also show that the yields of the main products of SN Ia nucleosynthesis do not depend on the details of which rates are modified, but can be parametrized by an observational quantity such as Ca/S. Using this SNR-calibrated approach, we then proceed to compute a new set of SN Ia models and nucleosynthesis for both Chandrasekhar and sub-Chandrasekhar mass progenitors with a one-dimensional hydrodynamics and nucleosynthesis code. We discuss the nucleosynthesis of the models as a function of progenitor metallicity, mass, and deflagration-to-detonation transition density. The yields of each model are almost independent on the reaction rates modified for a common Ca/S ratio.

**Key words:** hydrodynamics – nuclear reactions, nucleosynthesis, abundances – supernovae: general – white dwarfs

## 1 INTRODUCTION

Type Ia supernovae (SN Ia) are a fairly homogeneous class of high-luminosity transient phenomena whose spectra are characterized by the absence of lines from the most abundant elements in the Cosmos, hydrogen and helium, and the presence of a conspicuous silicon line at 6150 Å around maximum light (Minkowski 1939, 1941; Pskovskii 1969; Branch & Patchett 1973; Wheeler & Harkness 1986). They have been instrumental in the establishment of the current cosmological model, characterized by an accelerated expansion of the Universe, the measurement of the contribution of dark energy to the energy budget of the Universe, and constraining the equation of state of dark energy (e.g. Riess et al. 1998; Perlmutter et al. 1999; Riess et al. 2004; Wood-Vasey et al. 2007; Scolnic et al. 2018). But the imprints of SN Ia go beyond their applications as standard candles, and cover aspects as diverse as the evolution of the interstellar and intracluster media (Chevalier 1977; Sawala et al. 2010), the generation of cosmic rays (Warren et al. 2005; Sinitsyna &

Sinitsyna 2011; Takamoto & Kirk 2015; Cardillo et al. 2016), or the source of most stable isotopes of the elements of the iron-group (IGE) (Matteucci & Tornambe 1987; Matteucci et al. 2009; Maoz & Graur 2017; McWilliam et al. 2018; Prantzos et al. 2018).

The accepted progenitor of SN Ia is a carbon-oxygen (CO) white dwarf (WD) exploding as a consequence of destabilization due to mass accretion or whatever other cause. If the WD mass is close to the Chandrasekhar limit (Chandra scenario), the explosion can propagate either as a pure deflagration (Nomoto et al. 1984) or as a delayed detonation (DDT, Khokhlov 1991). If its mass is substantially below the Chandrasekhar limit (subCh scenario) the burning front propagates as a pure detonation (Woosley & Weaver 1994; Woosley & Kasen 2010; Sim et al. 2010). Hydrodynamical simulations of WD explosion can explain most of the features in the optical light curve and spectra of SN Ia, both in the Chandra and in the subCh scenarios (Nomoto 1984; Hoefflich et al. 1998; Woosley et al. 2007; Kasen et al. 2009; Blondin et al. 2013, 2017; Hoefflich et al. 2017). The light curve is most sensitive to the kinetic energy imparted to the ejecta and to the mass of  $^{56}\text{Ni}$  synthesized in the course

<sup>★</sup> E-mail: eduardo.bravo@upc.edu

of the thermonuclear explosion. The spectra are formed by many lines of intermediate-mass elements (IME) and IGE, but the interpretation in terms of the mass of each element present in the ejecta is not trivial (Branch et al. 2005; Stehle et al. 2005; Gerardy et al. 2007; Mazzali et al. 2008; Tanaka et al. 2011a; Sasdelli et al. 2014; Ashall et al. 2016).

The thermonuclear nature of SN Ia couples the nucleosynthesis with the explosion properties, but the direct impact on the optical of all but the major product of these explosions, the radioactive isotope  $^{56}\text{Ni}$ , is very limited. As a result, most of the nucleosynthesis predictions of current SN Ia models cannot be verified by the available optical data. Observations of close SN Ia for long periods of time put some constraints on their nucleosynthesis, although with large uncertainties (Diamond et al. 2015; Botyánszki & Kasen 2017; Dimitriadis et al. 2017; Graur et al. 2018; Maguire et al. 2018). The X-ray spectra of young SN Ia remnants (SNRs) allow more precision on the determination of mass ratios of several IME and IGE (Badenes et al. 2006, 2008; Park et al. 2013; Yang et al. 2013; Yamaguchi et al. 2015; Dave et al. 2017). Indeed, Martínez-Rodríguez et al. (2017) have determined the mass ratio of calcium to sulfur in several SN Ia remnants with relative errors in the range  $\sim 5\% - 16\%$ . Measurements in SNRs are easier because the plasma is optically thin and all the shocked ejecta are emitting radiation, allowing for a relatively simple correspondence between the emitted photons and the emitting mass.

Most nucleosynthesis calculations associated with SN Ia models have been performed using the technique of post-processing. In this technique, first a simplified nuclear network is used within the hydrodynamic solver, which allows to obtain the release of nuclear energy with enough accuracy to follow the hydrodynamic evolution of the explosion. In a second step, the detailed nuclear composition of the ejecta is computed using a large nuclear network, i.e. feeding a nuclear kinetic code with the thermodynamical trajectories of different WD zones along the explosion, computed using the simplified nuclear network (e.g. Thielemann et al. 1986; Bravo et al. 2010; Townsley et al. 2016; Leung & Nomoto 2017). This approach is unavoidable in multi-dimensional simulations of SN Ia because of the large requirements on CPU associated with resolving the hydrodynamical part of the problem, including flame propagation. However, nowadays it is possible to incorporate a large nuclear network in hydrocodes used in one-dimensional models of SN Ia (Miles et al. 2018).

The aim of the present work is twofold. First, we present our one-dimensional SN Ia explosion code, which uses a large nuclear network in the computation of the hydrodynamic evolution, allowing to obtain the detailed nuclear composition directly, without the need of post-processing, and ensuring full coherence between the explosion energetics and the nucleosynthesis. Second, we address the nucleosynthesis constraints derived from X-ray data on SN Ia remnants. Specifically, we explore the ways to match the constraints posed by the observations of calcium, argon, and sulfur in several remnants (Martínez-Rodríguez et al. 2017), allowing for reasonable uncertainties in several key reaction rates. We identify a combination of rates that satisfies the above constraints, and use this SNR-calibration to study the dependence of the nucleosynthesis on parameters such as the

progenitor metallicity, the WD mass, and the deflagration-to-detonation transition density.

The plan of the paper is as follows. In Section 2 we explain the general aspects of our method and related assumptions. In Section 3 we discuss the observational constraints posed by X-ray spectra. These constraints allow us to define the set of reaction rates adopted in our code. We discuss the nucleosynthesis in Section 4, and summarize our conclusions in Section 5. In Appendix A, we give the nucleosynthetic yields obtained with the standard set of reaction rates and, in Appendix B, we provide further technical details about the characteristics of our code and the way in which it incorporates an extensive nuclear network in the hydrodynamics modelling of SN Ia.

## 2 FRAMEWORK

We have computed SN Ia explosion models in spherical symmetry for sub-Chandrasekhar WD detonation and Chandra WD DDT. Our code integrates simultaneously the hydrodynamics, via a PPM solver, and the nuclear network. Here, we describe the general features of the models, and leave further technical details for appendix B.

In the subCh scenario, a carbon-oxygen WD with a mass significantly below the Chandrasekhar limit explodes through a detonation starting at its center. The detonation may be triggered by an inward shock wave launched at the surface by the burning of a tiny layer of helium (not present in our simulations) accreted from a degenerate or non-degenerate companion. The detonation might also be the consequence of a dynamic event (merging, collision) in a double-degenerate system. The exploding WD is characterized by its mass,  $M_{\text{WD}}$ , temperature,  $T_{\text{WD}}$ , and chemical composition. The initial chemical composition is set by the carbon-to-oxygen mass ratio (C/O) and the mass fraction of elements heavier than oxygen. This is equal to the metallicity,  $Z$ , of the progenitor star (Timmes et al. 2003), because during hydrostatic hydrogen and helium burning the amount of CNO at birth of the progenitor star is transformed into  $^{22}\text{Ne}$ . Besides  $^{12}\text{C}$ ,  $^{16}\text{O}$  and  $^{22}\text{Ne}$ , we complement the initial chemical composition with metals with baryon number  $23 \leq A \leq 100$ , which we assume are present in solar proportions (Grevesse & Noels 1993) with respect to  $Z$ .

In the Chandra DDT scenario, a carbon-oxygen WD with a mass close to the Chandrasekhar limit explodes, starting by a subsonic flame (deflagration) at or near its center. After consumption of a small fraction of the WD mass and expansion by a factor of  $\sim 2 - 6$  in radius, the burning fronts turns into a detonation that processes most of the star. The origin of the deflagration may be accretion of matter from a non-degenerate companion or from the debris of a degenerate companion after a merging event. Either way, the explosion is preceded by a long ( $\sim 10^3$  yrs) phase of slow carbon burning (usually referred to as simmering or smoldering), in which the chemical composition is altered with respect to that of the WD at its birth. These models are characterized by the value of the density ahead the flame at the moment in which the deflagration-to-detonation transition is induced,  $\rho_{\text{DDT}}$ , and also by the initial central density,  $\rho_c$ , temperature,  $T_{\text{WD}}$ , and chemical composition, which we specify as in the subCh models. However, due to the chemical processing

during carbon simmering, the actual composition of matter is expected to differ from solar proportions. The amount of carbon consumed during simmering may be as large as  $0.026\text{--}0.036\ M_{\odot}$  (Piersanti et al. 2017), depending on the initial metallicity, but its precise value is affected by the numerical treatment of the URCA process (Piersanti, priv. comm.; Martínez-Rodríguez et al. 2016; Schwab et al. 2017), so we do not include this effect in our initial models. We warn that the actual metallicity of the main-sequence progenitor of the exploding WD in the Chandra DDT scenario may be different from the  $Z$  of the models as reported in Table 1.

In all our models, we adopt  $C/O = 1^1$  and  $T_{\text{WD}} = 10^8\ \text{K}$ . All the initial models are built in hydrostatic equilibrium using the specified chemical composition. The central density of our Chandra DDT models is  $\rho_c = 3 \times 10^9\ \text{g cm}^{-3}$ , as suggested by models of the carbon simmering phase (Martínez-Rodríguez et al. 2016).

The thermonuclear reaction rates used in the simulations are those recommended by the REACLIB compilation (Cyburt et al. 2010), with electron screening in strong, intermediate and weak regimes, while weak interaction rates are adopted from Fuller et al. (1982); Oda et al. (1994); Martínez-Pinedo et al. (2000); Pruet & Fuller (2003). The exception is the  $^{12}\text{C}+^{16}\text{O}$  reaction.<sup>2</sup> We computed models with either the ‘standard’  $^{12}\text{C}+^{16}\text{O}$  reaction rate (Caughlan & Fowler 1988, hereafter CF88), or the same rate scaled down by a factor  $(1 - \xi_{\text{CO}})$ , with  $\xi_{\text{CO}} = 0.9$  to reproduce the Ca/S mass ratio in SNRs (Martínez-Rodríguez et al. 2017, see also Section 3 for more details). In both cases, we have adopted the CF88 branching ratios for the neutron, proton, and  $\alpha$  output channels.

The propagation model for the burning front is different depending on whether it is subsonic or supersonic. In the first case, i.e. for deflagration waves, the front is propagated at a fixed fraction of the local sound speed,  $v_{\text{def}} = 0.03v_{\text{sound}}$ . Once a detonation has been initiated, the front velocity is not prescribed, and the detonation advances as a result of the associated shock wave and the heat released by nuclear burning. The resulting detonation velocity is close to the Chapman-Jouguet value for the densities of interest, i.e.  $v_{\text{det}} \sim (1.1 - 1.3) \times 10^9\ \text{cm s}^{-1}$  for fuel densities  $\rho_{\text{fuel}} \leq 4 \times 10^7\ \text{g cm}^{-3}$  (Gamezo et al. 1999). The nucleosynthesis is mainly determined by the fuel density, see Fig. 1. In this figure, we have grouped all IME, here defined as those elements between and including magnesium and scandium, and all IGE to facilitate comparison with existing literature, e.g. figure A.1 in Fink et al. (2010), with which the agreement is quite satisfactory.

We present the hydrodynamic and nucleosynthesis output from 100 models, obtained by combining five values of  $\rho_{\text{DDT}}$ , five values of  $Z$ , and two parametrizations of the  $^{12}\text{C}+^{16}\text{O}$  reaction rate, for the Chandra models, and five values of  $M_{\text{WD}}$ , together with the same five values of  $Z$  and the two parametrizations of the  $^{12}\text{C}+^{16}\text{O}$  reaction rate, for the subCh models. Chandra models are named starting

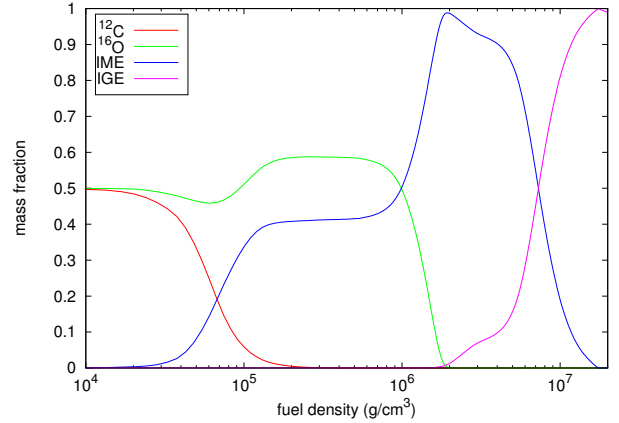


**Figure 1.** Nucleosynthetic yields as a function of density resulting from detonation of  $C/O$  in model 1p06\_Z2p25e-3\_std. We show the main constituents of the ejected matter, carbon, oxygen, IME, and IGE. Nevertheless, for fuel densities in the range  $4 \times 10^4 - 10^5\ \text{g cm}^{-3}$ , the abundance of neon (not plotted here) may be as large as  $\sim 16\%$  by mass.

by ‘ddt’, then the value of  $\rho_{\text{DDT}}$  in units of  $10^7\ \text{g cm}^{-3}$ , then ‘Z’ followed by the progenitor metallicity, then either ‘ $\xi_{\text{CO}}0\text{p9}$ ’ for the models ran with  $\xi_{\text{CO}} = 0.9$  or ‘std’ for the models ran with the standard CF88  $^{12}\text{C}+^{16}\text{O}$  reaction rate. For instance, model ‘ddt1p2\_Z2p25e-4\_ξCO0p9’ belongs to the delayed-detonation of a Chandrasekhar-mass WD with  $\rho_{\text{DDT}} = 1.2 \times 10^7\ \text{g cm}^{-3}$ , metallicity  $Z = 2.25 \times 10^{-4}$ , and  $\xi_{\text{CO}} = 0.9$ . On the other hand, subCh models are named starting with the value of the WD mass, in solar masses, then the metallicity and the treatment of the  $^{12}\text{C}+^{16}\text{O}$  reaction rate, as in Chandra models. For instance, model ‘1p06\_Z2p25e-3\_std’ belongs to the detonation of a sub-Chandrasekhar mass WD with  $M_{\text{WD}} = 1.06\ M_{\odot}$ , metallicity  $Z = 2.25 \times 10^{-3}$ , and  $\xi_{\text{CO}} = 0$ , i.e. the standard CF88  $^{12}\text{C}+^{16}\text{O}$  reaction rate.

The complete list of models is given in Table 1, as well as the final kinetic energy,  $K$ , and the ejected mass of  $^{56}\text{Ni}$ . We emphasize that the central density reported for the subCh models is a result of the construction of the initial models in hydrostatic equilibrium for given  $M_{\text{WD}}$  and  $Z$ . As a result, it reflects a slight dependence on the WD metallicity, especially for the most neutronized progenitors.

In Figs. 2 and 3, we show the evolution of a sample of models, one subCh and one Chandra. Density (contours) and temperature (color) are shown as functions of time and mass coordinate. The pure detonation nature of the subCh models make their evolution relatively simple: matter burns at the density it has in the initial model, as shown by the horizontal density contours before arrival of the detonation. The mass consumption rate is:  $\dot{M} = 4\pi\rho r^2 v_{\text{det}}$ , which scales as  $r^2$  near the center (constant fuel density) and declines after the front reaches regions with smaller density, hence smaller  $v_{\text{det}}$ . The detonation wave approaches the outermost layers of the WD after  $\sim 0.5\ \text{s}$ . The maximum temperature attained behind the detonation front is a declining function of fuel density, going from  $\sim 6 \times 10^9\ \text{K}$  close to the center to  $< 3 \times 10^9\ \text{K}$  close to the surface. Models characterized by a smaller central density also reach lower maximum temperatures.

<sup>1</sup> In this paper, we adopt the convention that the ratio of two element symbols, e.g.  $C/O$  or  $\text{Ca/S}$ , makes reference to the ratio of the corresponding masses throughout the ejecta.

<sup>2</sup> See Section 3.2 for an exploration of other modifications of reaction rates.

**Table 1.** Characteristics of the computed SN Ia models.

Chandrasekhar-mass DDT			models with $\xi_{\text{CO}} = 0.9$		models with $\xi_{\text{CO}} = 0$	
$\rho_{\text{DDT}}$ ( $\text{g cm}^{-3}$ )	$Z$	$\rho_c$ ( $\text{g cm}^{-3}$ )	$K$ ( $10^{51}$ erg)	$M(^{56}\text{Ni})$ ( $\text{M}_{\odot}$ )	$K$ ( $10^{51}$ erg)	$M(^{56}\text{Ni})$ ( $\text{M}_{\odot}$ )
$1.2 \times 10^7$	$2.25 \times 10^{-4}$	$3.0 \times 10^9$	1.193	0.316	1.170	0.269
$1.2 \times 10^7$	$2.25 \times 10^{-3}$	$3.0 \times 10^9$	1.185	0.303	1.169	0.266
$1.2 \times 10^7$	$9.00 \times 10^{-3}$	$3.0 \times 10^9$	1.182	0.293	1.165	0.251
$1.2 \times 10^7$	$2.25 \times 10^{-2}$	$3.0 \times 10^9$	1.158	0.250	1.139	0.214
$1.2 \times 10^7$	$6.75 \times 10^{-2}$	$3.0 \times 10^9$	1.138	0.188	1.131	0.185
$1.6 \times 10^7$	$2.25 \times 10^{-4}$	$3.0 \times 10^9$	1.328	0.517	1.317	0.491
$1.6 \times 10^7$	$2.25 \times 10^{-3}$	$3.0 \times 10^9$	1.323	0.510	1.314	0.487
$1.6 \times 10^7$	$9.00 \times 10^{-3}$	$3.0 \times 10^9$	1.307	0.476	1.292	0.443
$1.6 \times 10^7$	$2.25 \times 10^{-2}$	$3.0 \times 10^9$	1.287	0.434	1.285	0.426
$1.6 \times 10^7$	$6.75 \times 10^{-2}$	$3.0 \times 10^9$	1.277	0.366	1.277	0.368
$2.4 \times 10^7$	$2.25 \times 10^{-4}$	$3.0 \times 10^9$	1.447	0.750	1.433	0.716
$2.4 \times 10^7$	$2.25 \times 10^{-3}$	$3.0 \times 10^9$	1.443	0.743	1.429	0.710
$2.4 \times 10^7$	$9.00 \times 10^{-3}$	$3.0 \times 10^9$	1.429	0.704	1.420	0.685
$2.4 \times 10^7$	$2.25 \times 10^{-2}$	$3.0 \times 10^9$	1.413	0.663	1.409	0.655
$2.4 \times 10^7$	$6.75 \times 10^{-2}$	$3.0 \times 10^9$	1.389	0.549	1.385	0.546
$2.8 \times 10^7$	$2.25 \times 10^{-4}$	$3.0 \times 10^9$	1.468	0.804	1.457	0.780
$2.8 \times 10^7$	$2.25 \times 10^{-3}$	$3.0 \times 10^9$	1.463	0.794	1.451	0.767
$2.8 \times 10^7$	$9.00 \times 10^{-3}$	$3.0 \times 10^9$	1.453	0.765	1.447	0.754
$2.8 \times 10^7$	$2.25 \times 10^{-2}$	$3.0 \times 10^9$	1.437	0.721	1.431	0.707
$2.8 \times 10^7$	$6.75 \times 10^{-2}$	$3.0 \times 10^9$	1.412	0.595	1.410	0.596
$4.0 \times 10^7$	$2.25 \times 10^{-4}$	$3.0 \times 10^9$	1.507	0.909	1.500	0.896
$4.0 \times 10^7$	$2.25 \times 10^{-3}$	$3.0 \times 10^9$	1.503	0.902	1.497	0.891
$4.0 \times 10^7$	$9.00 \times 10^{-3}$	$3.0 \times 10^9$	1.493	0.872	1.487	0.859
$4.0 \times 10^7$	$2.25 \times 10^{-2}$	$3.0 \times 10^9$	1.478	0.824	1.475	0.817
$4.0 \times 10^7$	$6.75 \times 10^{-2}$	$3.0 \times 10^9$	1.456	0.689	1.454	0.688
sub-Chandrasekhar detonation			models with $\xi_{\text{CO}} = 0.9$		models with $\xi_{\text{CO}} = 0$	
$M_{\text{WD}}$ ( $\text{M}_{\odot}$ )	$Z$	$\rho_c$ ( $\text{g cm}^{-3}$ )	$K$ ( $10^{51}$ erg)	$M(^{56}\text{Ni})$ ( $\text{M}_{\odot}$ )	$K$ ( $10^{51}$ erg)	$M(^{56}\text{Ni})$ ( $\text{M}_{\odot}$ )
0.88	$2.25 \times 10^{-4}$	$0.15 \times 10^8$	0.926	0.191	0.907	0.150
0.88	$2.25 \times 10^{-3}$	$0.15 \times 10^8$	0.921	0.182	0.905	0.145
0.88	$9.00 \times 10^{-3}$	$0.15 \times 10^8$	0.917	0.169	0.904	0.138
0.88	$2.25 \times 10^{-2}$	$0.15 \times 10^8$	0.913	0.155	0.902	0.133
0.88	$6.75 \times 10^{-2}$	$0.16 \times 10^8$	0.926	0.139	0.920	0.133
0.97	$2.25 \times 10^{-4}$	$0.26 \times 10^8$	1.160	0.457	1.140	0.427
0.97	$2.25 \times 10^{-3}$	$0.26 \times 10^8$	1.150	0.449	1.140	0.421
0.97	$9.00 \times 10^{-3}$	$0.26 \times 10^8$	1.150	0.433	1.140	0.410
0.97	$2.25 \times 10^{-2}$	$0.27 \times 10^8$	1.140	0.412	1.130	0.395
0.97	$6.75 \times 10^{-2}$	$0.28 \times 10^8$	1.150	0.363	1.140	0.358
1.06	$2.25 \times 10^{-4}$	$0.47 \times 10^8$	1.330	0.706	1.320	0.685
1.06	$2.25 \times 10^{-3}$	$0.47 \times 10^8$	1.330	0.699	1.320	0.679
1.06	$9.00 \times 10^{-3}$	$0.48 \times 10^8$	1.320	0.680	1.320	0.664
1.06	$2.25 \times 10^{-2}$	$0.49 \times 10^8$	1.320	0.650	1.310	0.638
1.06	$6.75 \times 10^{-2}$	$0.52 \times 10^8$	1.320	0.569	1.320	0.565
1.10	$2.25 \times 10^{-4}$	$0.63 \times 10^8$	1.400	0.807	1.390	0.791
1.10	$2.25 \times 10^{-3}$	$0.63 \times 10^8$	1.390	0.801	1.390	0.785
1.10	$9.00 \times 10^{-3}$	$0.64 \times 10^8$	1.390	0.781	1.380	0.769
1.10	$2.25 \times 10^{-2}$	$0.65 \times 10^8$	1.380	0.748	1.380	0.739
1.10	$6.75 \times 10^{-2}$	$0.71 \times 10^8$	1.380	0.653	1.380	0.650
1.15	$2.25 \times 10^{-4}$	$0.94 \times 10^8$	1.470	0.928	1.460	0.918
1.15	$2.25 \times 10^{-3}$	$0.94 \times 10^8$	1.460	0.922	1.460	0.913
1.15	$9.00 \times 10^{-3}$	$0.95 \times 10^8$	1.460	0.901	1.460	0.894
1.15	$2.25 \times 10^{-2}$	$0.98 \times 10^8$	1.450	0.865	1.450	0.859
1.15	$6.75 \times 10^{-2}$	$1.07 \times 10^8$	1.450	0.753	1.450	0.751

The evolution of the Chandra DDT model is more involved. The explosion starts at the center of the WD as a deflagration and propagates for two seconds, consuming  $0.22 \text{ M}_{\odot}$  before changing into a detonation. Since the deflagration is subsonic, the star has time to expand before the arrival of the burning front. The expansion is communi-

cated gradually from the innermost to the outermost layers (density contours start bending downwards), and becomes global  $\sim 1 \text{ s}$  after thermal runaway. Once initiated, the detonation reaches almost the surface of the WD without apparent interference from the hydrodynamic processes inside. However, a close inspection of Fig. 3 reveals some ripples



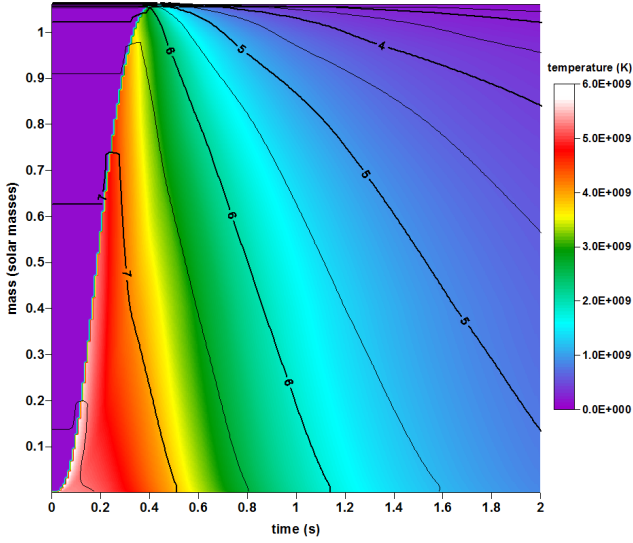


**Figure 2.** Evolution of temperature (color) and density (contours) as a function of time and mass coordinate in a sub-Chandrasekhar detonation model with  $M_{\text{WD}} = 1.06 M_{\odot}$  and metallicity  $Z = 0.009$ , model 1p06\_Z9e-3.std. The contour labels give the logarithm of the density.

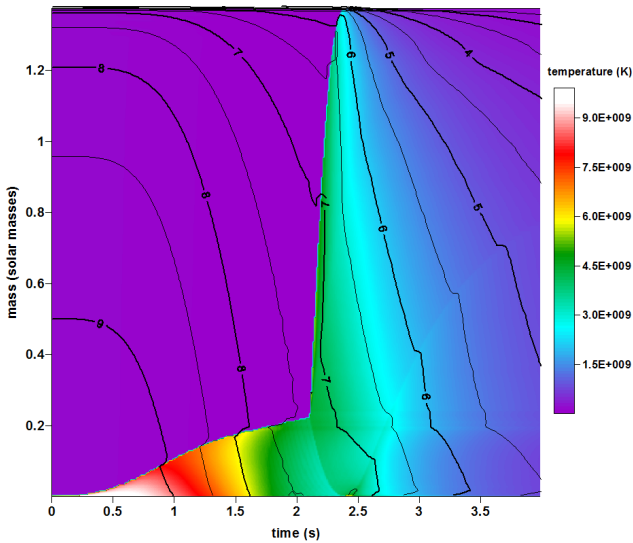


**Figure 3.** Same as Fig. 2, but for a Chandrasekhar-mass delayed detonation model with deflagration-to-detonation transition density  $\rho_{\text{DDT}} = 2.4 \times 10^7 \text{ g cm}^{-3}$  and metallicity  $Z = 0.009$ , model ddt2p4\_Z9e-3.std. Note that the color scale, as well as the x and y axes, are different than those of the previous figure.

in the density contours accompanied by subtle changes in temperature. The last are due to an inwards-moving shock wave, launched from the location of the detonation initiation, that reaches the center of the WD at  $\sim 2.4$  s and rebounds, moving outwards thereafter. Since our code solves simultaneously hydrodynamics and nuclear network, it incorporates the effects of all these waves on the evolution of the explosion.

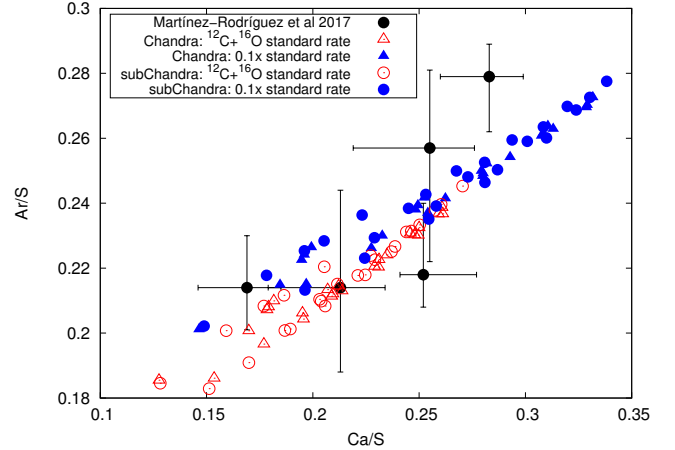


**Figure 4.** Measured abundance ratio of argon to sulfur vs calcium to sulfur in supernova remnants (big black dots with errorbars) compared with the predictions of our model set using either the standard  $^{12}\text{C}+^{16}\text{O}$  reaction rate (empty magenta symbols) or the same rate scaled down by a factor 10, i.e.  $\xi_{\text{CO}} = 0.9$  (solid blue symbols). The uppermost black point belongs to the *Kepler* SNR.

### 3 CALCIUM, SULFUR AND THE FUSION OF CARBON AND OXYGEN

Martínez-Rodríguez et al. (2017) argued that the Ca/S ratios measured in the X-ray spectra of Type Ia SNRs span values that are not reproduced by most SN Ia explosion models. These authors speculate that the cause may be the overestimation of the  $^{12}\text{C}+^{16}\text{O}$  reaction rate by a factor  $\sim 10$ , i.e.  $\xi_{\text{CO}} = 0.9$ . Fig. 4 shows Ca/S and Ar/S obtained with our SN Ia models, with either the standard rate of this reaction or  $\xi_{\text{CO}} = 0.9$ , compared with the abundance ratios measured by Martínez-Rodríguez et al. (2017). Models calculated with the standard rate of the  $^{12}\text{C}+^{16}\text{O}$  reaction are unable to reproduce both the Ar/S and the Ca/S ratios, in particular that of the *Kepler* SNR. On the other hand, models with  $\xi_{\text{CO}} = 0.9$  cover the whole range of observational points. However, the reduction of the rate of the reaction  $^{12}\text{C}+^{16}\text{O}$  by a factor of ten may be beyond the current experimental uncertainty of this rate, which Shen et al. (2018) estimate on the order of 50% at the temperatures of interest for explosive oxygen burning,  $T \sim (3.5\text{--}5) \times 10^9$  K.

#### 3.1 Impact of the $^{12}\text{C}+^{16}\text{O}$ reaction rate

Scaling-down the  $^{12}\text{C}+^{16}\text{O}$  reaction rate with  $\xi_{\text{CO}} = 0.9$  affects unevenly different elements present in the ejecta of SN Ia. The impact of this reaction rate on the yield of a given element can be understood by comparing the locations where the element is produced with the places where the reaction is most active. Fig. 5 shows the mass flux associated with the  $^{12}\text{C}+^{16}\text{O}$  reaction as a function of mass coordinate and time, for model 1p06\_Z9e-3.std. The flux is large in two regions, one between mass coordinates  $\sim 0.6$  and  $\sim 0.85 M_{\odot}$ , and the other outside of  $\sim 0.97 M_{\odot}$ , where the final mean molecular weights are 35–50 and  $< 30$ , respectively. Thus, we expect that IMEs and lighter elements are most sensitive to the  $^{12}\text{C}+^{16}\text{O}$  reaction rate.

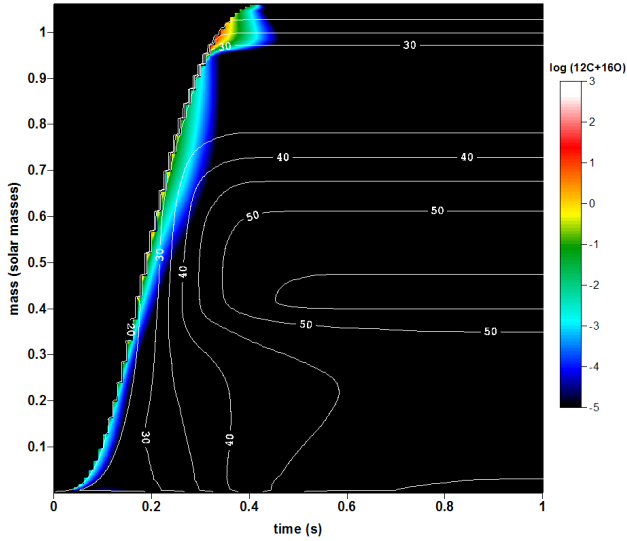


**Figure 5.** Time evolution of the mean molecular weight (contours) and the mass flux of the  $^{12}\text{C}+^{16}\text{O}$  reaction, given by  $28N_{\text{Av}}\rho < \sigma \cdot v > Y_{12\text{C}}Y_{16\text{O}}$  (color, logarithmic scale), for model 1p06\_Z9e-3\_std.

Fig. 6 is a map of the final distribution of each element in the ejecta of model 1p06\_Z9e-3\_std, normalized to the total yield of the same element, thus, going from 0 at the center (brown) to 1 at the surface (red). The two horizontal dotted lines limit the region where conditions for explosive oxygen burning are achieved. It can be seen that several groups of elements are synthesized in similar regions of the white dwarf. For instance, most odd- $Z$  IMEs are produced in the outermost 10-15% of the star, while most even- $Z$  IMEs and the lightest IGEs, from titanium to manganese, are created in the outer half of the white dwarf.

Elements from the iron-group are mostly produced in the innermost regions of the WD, and their yield is hardly influenced by the rate of the  $^{12}\text{C}+^{16}\text{O}$  reaction. On the other hand, nitrogen, silicon, argon, calcium, and scandium are produced in the zones of maximal influence of this reaction, and within the regions that experience explosive oxygen burning. Sulfur is particular, in the sense that its region of maximal productivity coincides with the gap in the mass flux associated with the  $^{12}\text{C}+^{16}\text{O}$  reaction (Fig. 5), i.e. more than half the yield of sulfur in Fig. 6 is concentrated in between the mass range from  $0.85 M_{\odot}$  to  $0.97 M_{\odot}$ . The yields of other elements that are preferentially synthesized in the outermost regions of the WD are sensitive to this reaction rate, but are not a product of explosive oxygen burning and their abundances are, in general, very small. This is the case, for instance, of potassium and chlorine.

Figure 7 shows the same kind of map, pertaining to a Chandra model. Qualitatively, the distribution of yields is similar to that of the subCh model, although in the Chandra model the lightest IGE are synthesized closer to the center, while copper and zinc are synthesized very close to the surface of the WD.

Fig. 8 shows the relative changes introduced in the yields of the model with  $M_{\text{WD}} = 1.06 M_{\odot}$  and  $Z = 0.009$  (coloured points), when  $\xi_{\text{CO}} = 0.9$ . The variations remain

under 10% for IGE and sulfur, while calcium, argon, and silicon are most affected among the elements with largest yields. The results for other explosion models (not shown in Fig. 8) are similar.

The isotopic contribution to the abundance of each element is not affected by the rate of the  $^{12}\text{C}+^{16}\text{O}$  reaction as much as the yield of the elements is, for the same model. Figure 9 shows the percent contribution of each isotope to the abundance of its element when the standard reaction rate is used and when  $\xi_{\text{CO}} = 0.9$ . In contrast with elemental mass yields, which change up to 40%, the percent contribution of each isotope is largely insensitive to the rate of  $^{12}\text{C}+^{16}\text{O}$ , with the exception of  $^{54}\text{Cr}$ , whose contribution to chromium varies by as much as  $\sim 30\%$ .

### 3.2 Other reactions involving carbon and oxygen

The role of the reaction  $^{12}\text{C}+^{16}\text{O}$  in the synthesis of IME during *explosive oxygen burning* was highlighted by Woosley et al. (1971) nearly five decades ago. They showed that the key point is the regulation of  $\alpha$  particles produced per  $^{28}\text{Si}$  nucleus, a process that is contributed by four reactions involving  $^{12}\text{C}$  and  $^{16}\text{O}$ : three fusion reactions,  $^{12}\text{C}+^{12}\text{C}$ ,  $^{12}\text{C}+^{16}\text{O}$ , and  $^{16}\text{O}+^{16}\text{O}$ , plus the photodisintegration reaction  $^{16}\text{O}+\gamma \rightarrow ^{12}\text{C}+\alpha$ . The last two reactions provide the main paths of destruction of oxygen. If  $^{16}\text{O}+\gamma \rightarrow ^{12}\text{C}+\alpha$  is followed by  $^{12}\text{C}+^{12}\text{C} \rightarrow ^{20}\text{Ne}+\alpha$  and by  $^{20}\text{Ne}+\gamma \rightarrow ^{16}\text{O}+\alpha$ , the net effect is the release of four  $\alpha$  particles at the expense of one  $^{16}\text{O}$  nucleus. Otherwise, the destruction of  $^{16}\text{O}$ , either directly through  $^{16}\text{O}+^{16}\text{O}$  or indirectly by  $^{12}\text{C}+^{16}\text{O}$  just releases one  $\alpha$  particle per each pair of  $^{16}\text{O}$  nuclei consumed. Thus, two reactions contribute positively to a large  $\alpha$  abundance,  $^{16}\text{O}(\gamma, \alpha)$  and  $^{12}\text{C}+^{12}\text{C}$ , and two contribute negatively,  $^{12}\text{C}+^{16}\text{O}$  and  $^{16}\text{O}+^{16}\text{O}$ . It is possible that a combination of relatively minor changes in the rates of these reactions might have the same net effect on the final Ca/S and Ar/S ratios as the scaling down of the  $^{12}\text{C}+^{16}\text{O}$  reaction rate by a factor ten.

We have explored the results of modifying the four reaction rates by computing a set of 135 additional versions of model 1p06\_Z9e-3. In each model, the three fusion reaction rates were multiplied by a random factor in the range (0.5–1.5). To test the sensitivity to the rate of the photodisintegration reaction  $^{16}\text{O}(\gamma, \alpha)^{12}\text{C}$  (and its inverse), we used different rates (Caughlan et al. 1985; Caughlan & Fowler 1988; Buchmann 1996; Katsuma 2012; Xu et al. 2013) available in the JINA REACLIB database<sup>3</sup>. The behaviour of the last reaction rate at temperatures in excess of  $4 \times 10^9$  K is complicated and uncertain because of the possible contribution of high-energy resonances and cascade transitions (deBoer et al. 2017), and the use of different rates proposed in the literature is a convenient way to account for this uncertainty.

The resulting ratios of Ca/S, Si/Fe and Ti/Fe in these explosion models are shown by open circles in Fig. 10, and cover a range of Ca/S between 0.21 and 0.26. These figures can be compared with the ratios obtained for model 1p06\_Z9e-3\_std, with all standard rates (red solid pentagons, located at Ca/S=0.22), and for model 1p06\_Z9e-3- $\xi_{\text{CO}}0p9$ ,

<sup>3</sup> <https://groups.nsl.msui.edu/jina/reaclib/db/>

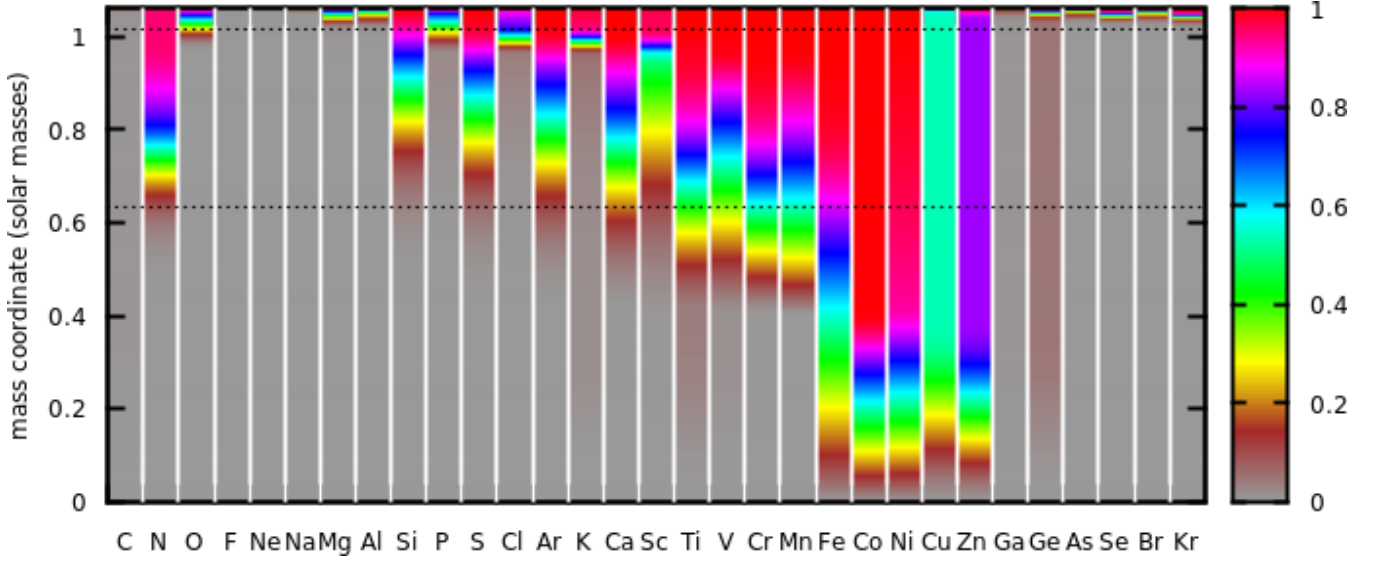


**Figure 6.** Final distribution of each element through the ejecta in model 1p06\_Z9e-3\_std. The color represents the cumulated mass of each element, starting from the center of the star, normalized to the total ejected mass of the same element. All elements go through light brown at the center to red at the surface, although this is not apparent for several elements whose yield is strongly concentrated in the outermost layers of the ejecta, e.g. carbon or gallium. The two black dashed lines enclose the region where the maximum temperature achieved by matter is in the range  $3.5 \leq T_{9,\max} \leq 5.0$ , in units of  $10^9$  K.

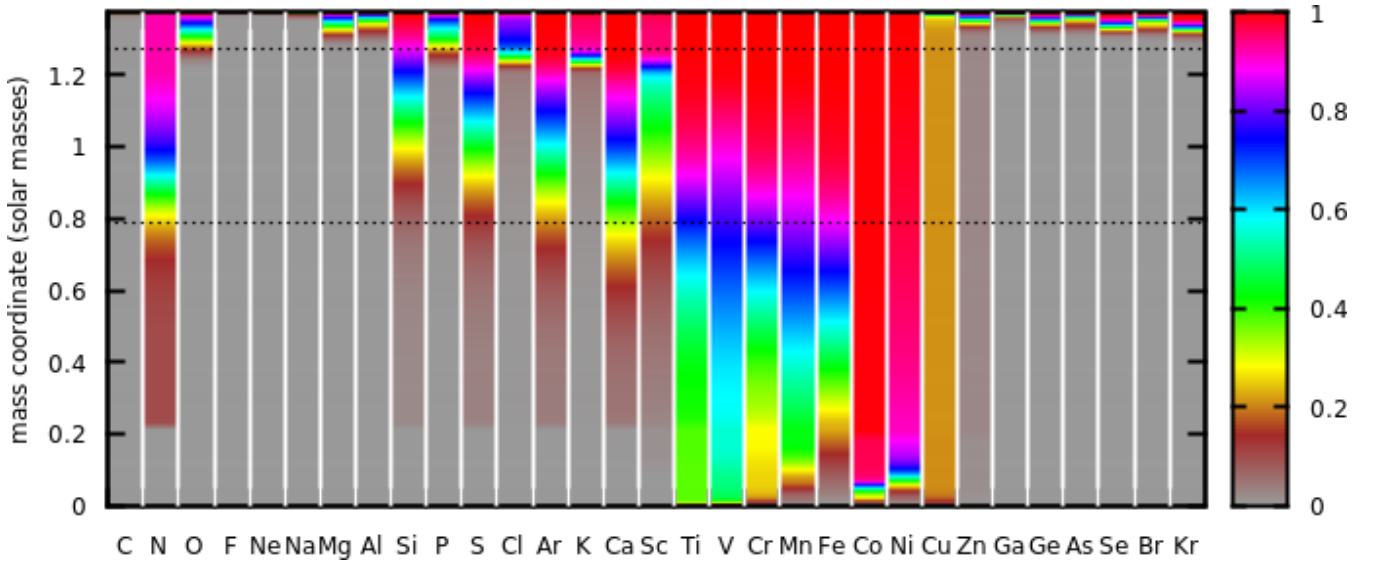


**Figure 7.** Same as Fig. 6 but for model ddt2p4\_Z9e-3\_std.

with all reactions but  $^{12}\text{C}+^{16}\text{O}$  given by the standard rates (green solid circles, located at  $\text{Ca}/\text{S}=0.273$ ). The abundance ratios show an almost linear monotonic dependence on each other, irrespective of what reaction rate was modified and in which measure. In other words, the ratios of  $\text{Si}/\text{Fe}$  and  $\text{Ti}/\text{Fe}$  can be specified, for an explosion model like 1p06\_Z9e-3, as a function of  $\text{Ca}/\text{S}$ , which is a quantity measurable in supernova remnants.

Motivated by these results, we have modified the four reaction rates involving carbon and oxygen in order to obtain  $\text{Ca}/\text{S}$  ratios similar to those for  $\xi_{\text{CO}} = 0.9$ , the value favoured

by SNR measurements. For model 1p06\_Z9e-3\_ $\xi_{\text{CO}}0.9$ , this means  $\text{Ca}/\text{S} \sim 0.27 - 0.28$ . For this experiment, we have had to change the four carbon and oxygen reaction rates by more than the 50% variations shown thus far.

Let us define a parameter to describe the scaling of each one of these reactions, similar to the definition of  $\xi_{\text{CO}}$  in Section 2. Thus, the rate of  $^{12}\text{C}+^{12}\text{C}$  is that from CF88 scaled by a factor  $(1 - \xi_{\text{CC}})$ , the rate of  $^{16}\text{O}+^{16}\text{O}$  is that from CF88 scaled by a factor  $(1 - \xi_{\text{OO}})$  and, finally, the meaning of  $\xi_{\text{CO}}$  is the same as before. The parameters of the four models with these rates modified are given in Table 2. In all

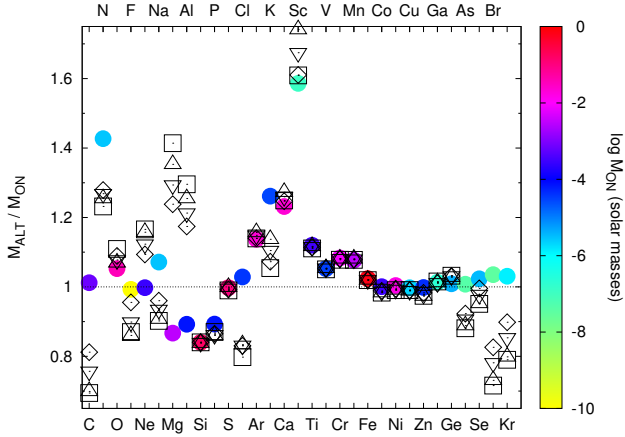


**Figure 8.** Relative change in the elemental yields derived from using alternative reaction rates ( $M_{\text{ALT}}$ ) instead of the standard ones ( $M_{\text{ON}}$ , model 1p06\_Z9e-3\_std). The solid coloured circles belong to model 1p06\_Z9e-3\_ξCO0p9, and the colour is assigned as a function of the yield of each element in model 1p06\_Z9e-3\_std. The rest of symbols belong to different combinations of modified rates of the reactions  $^{12}\text{C}+^{16}\text{O}$ ,  $^{12}\text{C}+^{12}\text{C}$ ,  $^{16}\text{O}+^{16}\text{O}$ , as well as  $^{12}\text{C}(\alpha, \gamma)^{16}\text{O}$  and its inverse, crafted to obtain similar ratios of calcium to sulfur yields (squares: model 1p06\_Z9e-3\_A, upward triangles: model 1p06\_Z9e-3\_B, downward triangles: model 1p06\_Z9e-3\_C, diamonds: model 1p06\_Z9e-3\_D, see Section 3.2 for further details).

**Table 2.** Parameters of the four models with modified rates of reactions involving carbon and oxygen.

model name	ξ <sub>CC</sub>	ξ <sub>OO</sub>	ξ <sub>CO</sub>
1p06_Z9e-3_A	-2.2	0.5	0.5
1p06_Z9e-3_B	-1.5	0.6	0.5
1p06_Z9e-3_C	-1.0	0.7	0.5
1p06_Z9e-3_D	-2.3	0.7	0.4

four models, the rates of  $^{16}\text{O}(\gamma, \alpha)^{12}\text{C}$  and its inverse were based on Katsuma (2012).

The point here is to explore to which extent fixing the Ca/S ratio in a given model, with respect to the variations in the rates of the carbon and oxygen reactions, is enough to determine the whole nucleosynthesis output or whether, on the contrary, the yields are sensitive to the precise reaction rates modified. The results of the four modified models are depicted in Fig. 10 as triangles, diamonds, and squares, close to the desired values, i.e. those of model 1p06\_Z9e-3\_ξCO0p9 (green solid circles).

The full yields of the four crafted models can be seen as well in Fig. 8 as open symbols, to be compared with the ratios obtained for model 1p06\_Z9e-3\_ξCO0p9 (coloured solid circles). Besides IGE, whose yields we already have shown that are not affected by the modified rates, the abundance ratios of elements which have an important contribution from explosive oxygen burning (see Figs. 6 and 7) are insensitive to the precise changes applied to the four reaction rates. To summarize, the combined variation of the rates in four key reactions involving  $^{12}\text{C}$  and  $^{16}\text{O}$  ( $^{12}\text{C}+^{16}\text{O}$ ,  $^{12}\text{C}+^{12}\text{C}$ ,  $^{16}\text{O}+^{16}\text{O}$ , and  $^{16}\text{O}+\gamma \rightarrow ^{12}\text{C}+\alpha$ ) within their uncertainties can have the same effect than the suppression of the rate

of the single reaction  $^{12}\text{C}+^{16}\text{O}$  by a factor  $\xi_{\text{CO}} = 0.9$ . In practice, this is true for the most important nucleosynthetic products of SN Ia, i.e. IGE and IME, with the exception of potassium and chlorine. These two elements are not a main product of explosive oxygen burning in our models, so their sensitivity to the four reaction rates is different from that of the products of this nucleosynthetic process (see Section 3.1).

One can wonder whether the exceptions to the above rule can provide a way to discriminate which ones of the four reactions should change with respect to their standard rates, and in which amount. This question is beyond the scope of the present paper and will need further investigation, but we can advance a few ideas. One possibility is to measure the ratio of two elements in SNRs, one which is sensitive to the changes in the four reaction rates and the other which is insensitive. For the first one, the first option that comes to mind is potassium, whose yield varies by  $\sim 30\%$  in Fig. 8 and is produced in non-negligible amounts in the explosion. For the second one, a good choice could be calcium, whose yield range of variation is on the order of a few percent. Even though the changes in the yield of potassium are modest, future mid-term projected X-ray facilities with spectroscopic capabilities like *XRISM* (with  $\sim 5$  eV energy resolution and  $\sim 300$  cm<sup>2</sup> effective area; Tashiro et al. 2018; Hitomi Collaboration et al. 2018) and *Athena* (with  $\sim 2.5$  eV energy resolution and an effective area close to 1 m<sup>2</sup>; Nandra et al. 2013) should be able to discriminate them.

## 4 YIELDS OF SNR-CALIBRATED SN IA MODELS

In this Section, we give the final (after radioactive decays) elemental and isotopic yields of the SN Ia models obtained with  $\xi_{\text{CO}} = 0.9$ . We have shown that these models are representative of a class of models in which the rates of the four reactions involving  $^{12}\text{C}$  and  $^{16}\text{O}$  may change by different amounts but have in common the abundance ratio of calcium to sulfur and that of argon to sulfur, and are, in this sense, SNR-calibrated SN Ia models. In Section 4.3, we give the yields, in solar masses, of the most abundant radioactive isotopes with half-life longer than one day. For completeness, we also give in Appendix A the yields of the models using the standard set of reaction rates,  $^{12}\text{C}+^{16}\text{O}$  included.

### 4.1 Chandrasekhar-mass models

The yields belonging to the Chandra models are given in Table 3. Rows starting by ‘elem’ give the elemental yields of each model, in solar masses, where the element is identified by the atomic number and symbol. Rows starting by ‘isot’ give the yield of each isotope in each model. In this case, the isotope is identified by the atomic number and symbol and by the baryon number.

The behaviour of the yields of the most abundant explosion products with respect to variations of the parameters of the Chandra models,  $\rho_{\text{DDT}}$  and  $Z$ , is illustrated in Figs. 11 and 12 (elements) and 13 and 14 (isotopes). It should be noted that the abundance scales are normalized to iron (and to the solar ratio), which means that a change in the relative abundance with, for instance,  $\rho_{\text{DDT}}$



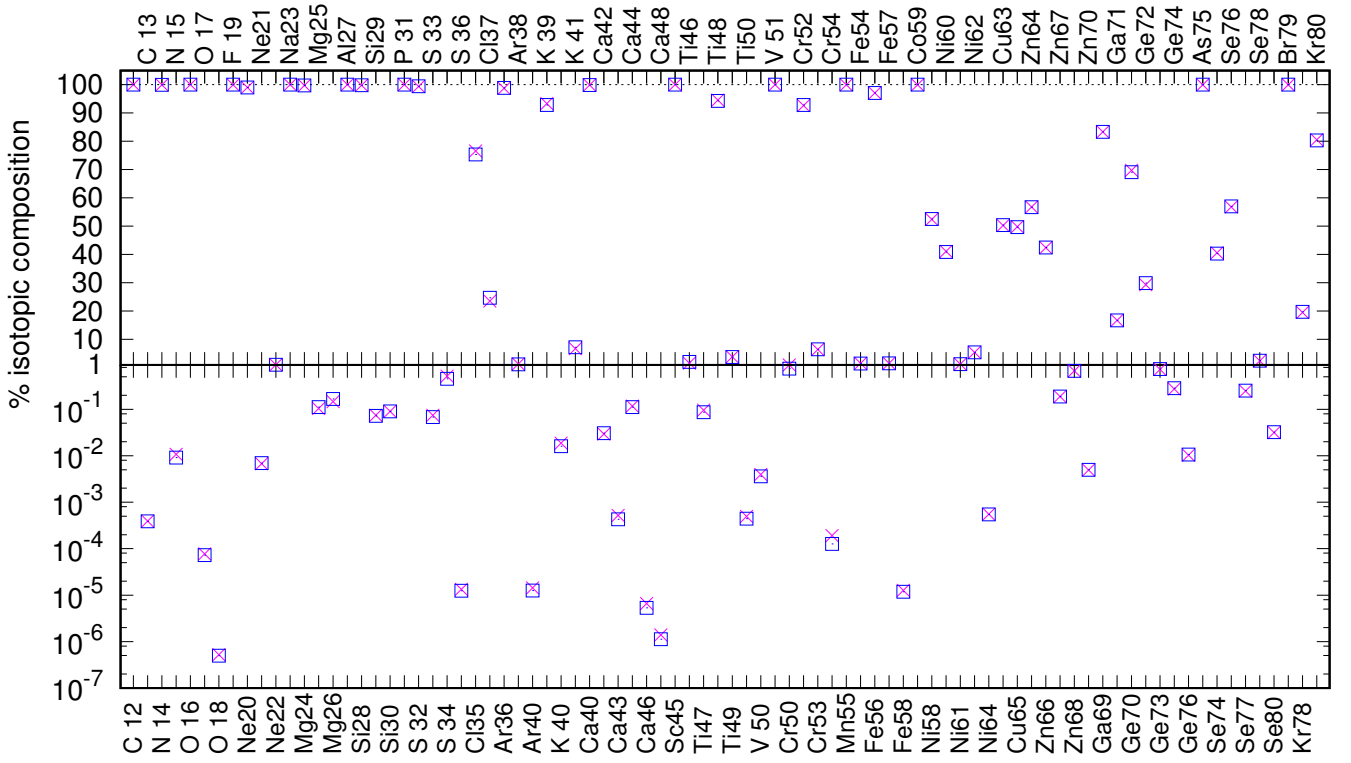


**Figure 9.** Percent isotopic contribution to the abundance of each element in models 1p06\_Z9e-3\_std (red crosses) and 1p06\_Z9e-3\_ξCO0p9 (blue empty squares). This plot shows that the distribution of the yield of each element among its different stable isotopes is practically independent of the rate of the reaction  $^{12}\text{C}+^{16}\text{O}$ .

**Table 3.** Nucleosynthesis in Chandrasekhar-mass DDT models with  $\xi_{\text{CO}} = 0.9$ .

$\rho_{\text{DDT}}$		1.2E+07	1.2E+07	1.2E+07	1.2E+07	1.2E+07	1.6E+07	1.6E+07	1.6E+07	1.6E+07	1.6E+07
$Z$		2.25E-4	2.25E-3	9.00E-3	2.25E-2	6.75E-2	2.25E-4	2.25E-3	9.00E-3	2.25E-2	6.75E-2
elem	2He	3.01E-04	2.87E-04	2.57E-04	1.61E-04	9.74E-06	3.08E-04	2.93E-04	2.62E-04	1.63E-04	9.43E-06
isot	2He3	1.58E-12	1.56E-12	1.54E-12	1.42E-12	1.16E-12	1.58E-12	1.56E-12	1.54E-12	1.42E-12	1.16E-12
isot	2He4	3.01E-04	2.87E-04	2.57E-04	1.61E-04	9.74E-06	3.07E-04	2.93E-04	2.62E-04	1.63E-04	9.43E-06
elem	6C	4.94E-03	4.98E-03	4.90E-03	5.06E-03	5.21E-03	2.50E-03	2.47E-03	2.54E-03	2.64E-03	2.51E-03
isot	6C12	4.94E-03	4.98E-03	4.90E-03	5.05E-03	5.21E-03	2.50E-03	2.47E-03	2.54E-03	2.64E-03	2.51E-03
isot	6C13	1.94E-10	3.57E-09	1.26E-08	2.95E-08	7.43E-08	1.04E-10	1.64E-09	6.37E-09	1.57E-08	3.94E-08

Sample of Table 3, the full version is available online. The meaning of the columns is explained in the text.

**Table 4.** Nucleosynthesis in sub-Chandrasekhar models with  $\xi_{\text{CO}} = 0.9$ .

$M_{\text{WD}}$		0.88	0.88	0.88	0.88	0.88	0.97	0.97	0.97	0.97	0.97
$Z$		2.25E-4	2.25E-3	9.00E-3	2.25E-2	6.75E-2	2.25E-4	2.25E-3	9.00E-3	2.25E-2	6.75E-2
elem	2He	1.95E-07	1.94E-07	1.73E-07	1.30E-07	1.02E-08	2.21E-04	2.34E-04	2.67E-04	3.31E-04	4.90E-04
isot	2He3	1.76E-16	1.76E-16	1.78E-16	1.83E-16	2.15E-16	6.37E-16	6.31E-16	6.14E-16	5.81E-16	4.83E-16
isot	2He4	1.95E-07	1.94E-07	1.73E-07	1.29E-07	1.02E-08	2.20E-04	2.34E-04	2.67E-04	3.31E-04	4.90E-04
elem	6C	4.04E-03	4.03E-03	3.96E-03	3.82E-03	3.35E-03	1.67E-03	1.66E-03	1.63E-03	1.57E-03	1.37E-03
isot	6C12	4.04E-03	4.03E-03	3.96E-03	3.82E-03	3.34E-03	1.67E-03	1.66E-03	1.63E-03	1.56E-03	1.37E-03
isot	6C13	2.20E-10	3.65E-09	1.21E-08	2.59E-08	5.61E-08	9.51E-11	1.52E-09	5.65E-09	1.28E-08	2.83E-08

Sample of Table 4, the full version is available online. The meaning of the columns is the same as in Table 3.

may be due to a varying iron yield, to a change in the element yield, or to both. In these figures, the dependence on metallicity is illustrated taking as a reference the models with  $\rho_{\text{DDT}} = 2.4 \times 10^7 \text{ g cm}^{-3}$ , whose  $^{56}\text{Ni}$  yields are representative of normal-luminosity SN Ia.

The most remarkable feature in Fig. 12 is that the ratios of all elements, with respect to iron, decrease monotonously

with increasing deflagration-to-detonation transition density. It is a consequence of the increasing mass of IGE with increasing  $\rho_{\text{DDT}}$ , at given metallicity. Furthermore, most of the additional mass that is processed by nuclear reactions above the DDT layer is made of iron. Thus, all elements but iron show similar dependence on  $\rho_{\text{DDT}}$ . Manganese, chromium, and nickel are produced in almost solar

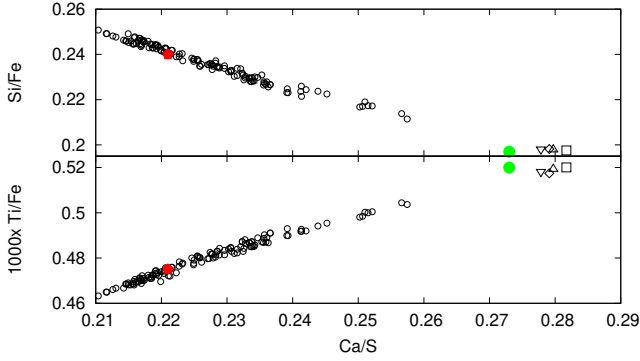


**Figure 10.** Variation in the ratios of silicon to iron and of titanium to iron vs the ratio of calcium to sulfur for a set of 139 models using random modifications of the reaction rates for  $^{12}\text{C}+^{16}\text{O}$ ,  $^{12}\text{C}+^{12}\text{C}$ ,  $^{16}\text{O}+^{16}\text{O}$ , and for  $^{12}\text{C}(\alpha, \gamma)^{16}\text{O}$  and its inverse. All models shown here are variants of the subCh model with  $M_{\text{WD}} = 1.06 M_{\odot}$  and  $Z = 0.009$ . Red solid pentagons belong to model 1p06\_Z9e-3\_std, i.e. with all standard rates, while green solid circles belong to model 1p06\_Z9e-3\_ξCO0p9, which reproduces the Ca/S and Ar/S mass ratios in SNRs. Open circles belong to models obtained with the rates of the three fusion reactions above multiplied by a random factor in the range (0.5–1.5), and the rate of photodisintegration of  $^{16}\text{O}$  given by alternate recipes in the JINA REACLIB database. The rest of symbols belong to models 1p06\_Z9e-3\_A (squares), 1p06\_Z9e-3\_B (upward triangles), 1p06\_Z9e-3\_C (downward triangles), and 1p06\_Z9e-3\_D (diamonds), see text and Table 2 for details.

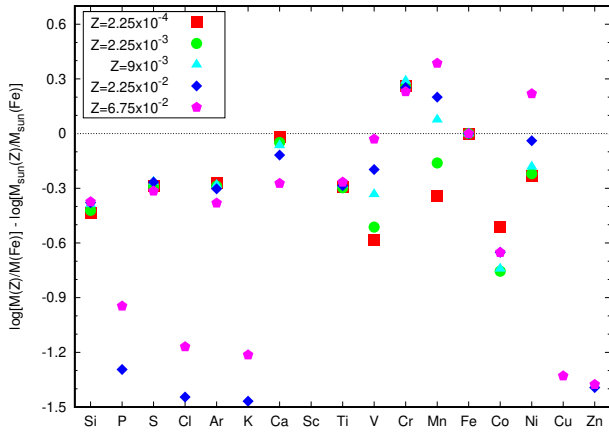


**Figure 11.** Variation of the elemental yields with respect to metallicity, for the Chandrasekhar-mass models with  $\rho_{\text{DDT}} = 2.4 \times 10^7 \text{ g cm}^{-3}$  and  $\xi_{\text{CO}} = 0.9$ . The yields are normalized to Fe and to the solar abundances, in log scale.

proportions with respect to iron in the most luminous models, i.e. those with the largest  $^{56}\text{Ni}$  yields. The same is true for titanium and vanadium in the most subluminescent models. The yields of a few elements, such as zinc, do not change monotonously with  $\rho_{\text{DDT}}$ . The only intermediate-mass elements produced in abundance are the even-atomic number ones: silicon, sulfur, argon, and calcium. They are even over-produced, with respect to iron and the solar proportions, in the most subluminescent models. On the other hand, scandium is under-abundant in all present models.

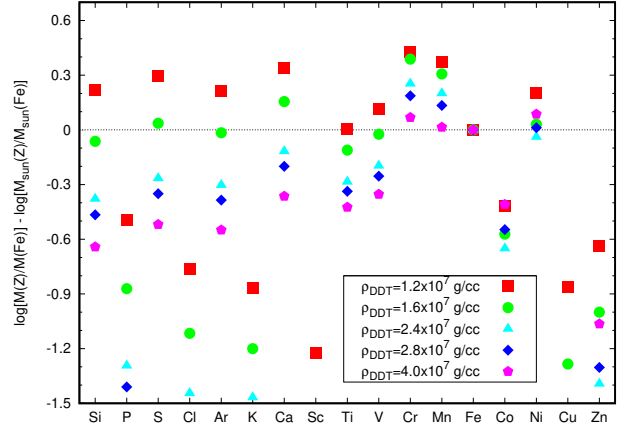


**Figure 12.** Variation of the elemental yields with respect to  $\rho_{\text{DDT}}$ , for the models with  $Z = 0.0225$  and  $\xi_{\text{CO}} = 0.9$ . The yields are normalized to Fe and to the solar abundances, in log scale.

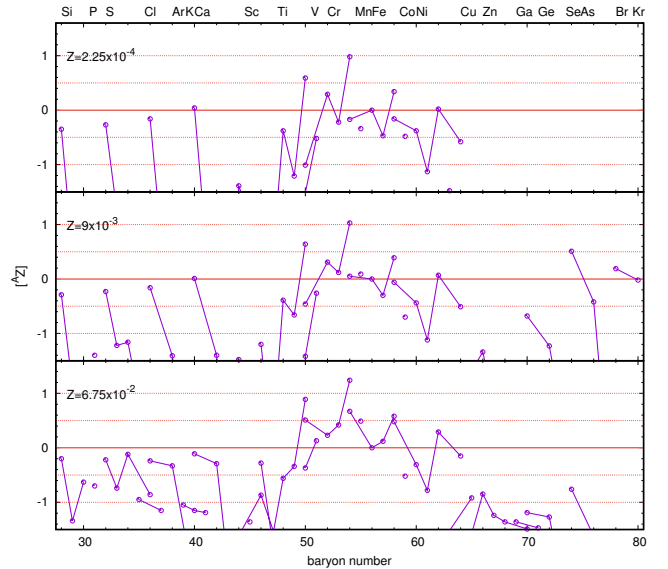


**Figure 13.** Variation of the isotopic yields with respect to metallicity, for the Chandrasekhar-mass models with  $\rho_{\text{DDT}} = 2.4 \times 10^7 \text{ g cm}^{-3}$  and  $\xi_{\text{CO}} = 0.9$ . The yields are normalized to  $^{56}\text{Fe}$  and to the solar abundances, in log scale. The approximate locus of each element is labelled on the top axis.

The variation of the mass ratios of the different elements with respect to metallicity does not behave as homogeneously as with respect to  $\rho_{\text{DDT}}$ . As can be appreciated in Fig. 11, by increasing  $Z$  one obtains larger yields of the odd-atomic number elements, with the exception of cobalt, while most of the even-atomic number ones remain largely unaffected, with the exception of nickel. Thus, the mass ratio of odd-to-even atomic number elements is, in general, sensitive to the progenitor metallicity, a result that has been already used to measure the metallicity of supernova progenitors through the ejecta abundances in supernova remnants (e.g. Badenes et al. 2008). The mass ratio of potassium to calcium is affected by the progenitor metallicity, so one has

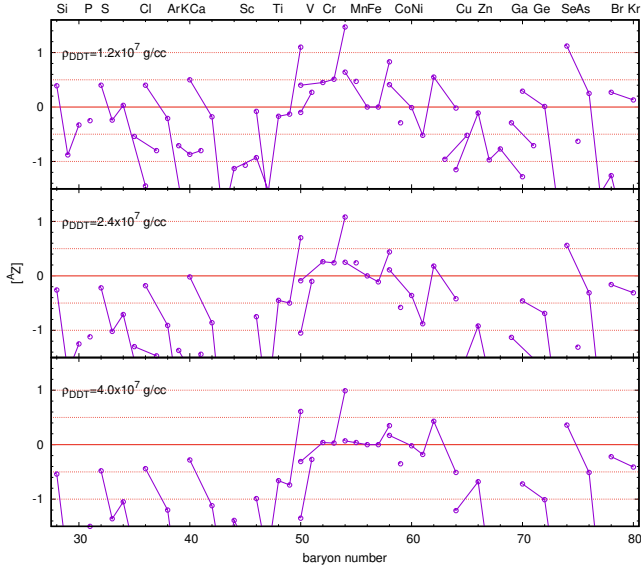


**Figure 14.** Variation of the isotopic yields with respect to  $\rho_{\text{DDT}}$ , for the models with  $Z = 0.0225$  and  $\xi_{\text{CO}} = 0.9$ . The yields are normalized to  $^{56}\text{Fe}$  and to the solar abundances, in log scale. The approximate locus of each element is labelled on the top axis.

to fix the last in order to use this mass ratio to get insight on the rate of the reactions involving carbon and oxygen, as explained in the previous section.

Isotopic mass ratios can not be directly measured in supernova remnants, but they are necessary ingredients in galactic chemical evolution models. In Figs. 13 and 14, we show the isotopic ratios for baryon number  $A \geq 28$ . Most isotopes from chromium to nickel are produced in almost solar proportions in the most luminous models (Fig. 14). The exceptions are  $^{50}\text{Ti}$ ,  $^{54}\text{Cr}$ ,  $^{58}\text{Fe}$ , and, to a lesser extent,  $^{62}\text{Ni}$ , which are overproduced in all models. This is due to the relatively high central density of the explosion models,  $\rho_c = 3 \times 10^9 \text{ g cm}^{-3}$ , which implies that matter is efficiently neutronized by electron captures on IGE isotopes in nuclear statistical equilibrium, shortly after central incineration, during the deflagration phase of the explosion. The isotope  $^{74}\text{Se}$  is overproduced at all  $\rho_{\text{DDT}}$  in models with metallicity ranging from slightly subsolar to slightly super-solar (Fig. 13). In the same metallicity range, the krypton isotopes  $^{78}\text{Kr}$  and  $^{80}\text{Kr}$  are produced in almost solar proportions with respect to  $^{56}\text{Fe}$ .

The isotopes that are most sensitive to  $Z$  are  $^{46}\text{Ti}$ ,  $^{49}\text{Ti}$ ,  $^{50}\text{V}$ ,  $^{51}\text{V}$ ,  $^{50}\text{Cr}$ ,  $^{53}\text{Cr}$ ,  $^{55}\text{Mn}$ ,  $^{54}\text{Fe}$ ,  $^{57}\text{Fe}$ , and  $^{58}\text{Ni}$ . We note that odd-baryon number and even-baryon number isotopes are equally represented in this list. Thus, the dependence of these isotope yields with respect to metallicity should be taken into account in chemical evolution models.

## 4.2 Sub-Chandrasekhar models

The yields belonging to the sub Chandrasekhar-mass models are given in Table 4, and illustrated in Figs. 15 to 18. In these figures, the dependence on metallicity is illustrated taking as a reference the models with  $M_{\text{WD}} = 0.97 M_{\odot}$ , whose  $^{56}\text{Ni}$  yields are representative of slightly sub-luminous SN Ia.

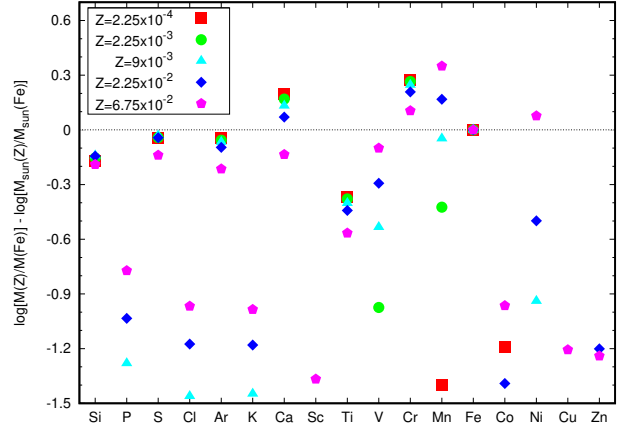


**Figure 15.** Variation of the elemental yields with respect to metallicity, for the sub-Chandrasekhar models with  $M_{\text{WD}} = 0.97 M_{\odot}$  and  $\xi_{\text{CO}} = 0.9$ .

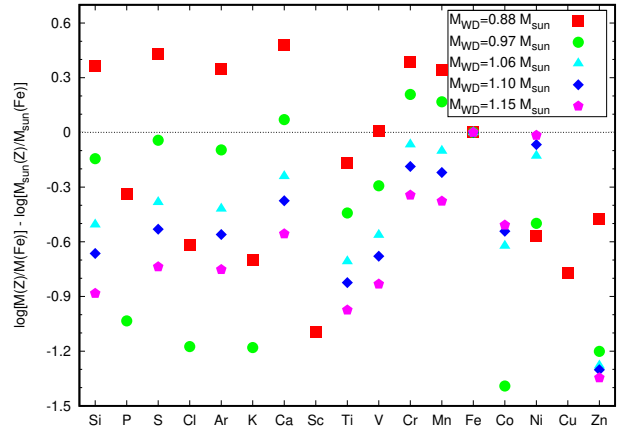


**Figure 16.** Variation of the elemental yields with respect to the WD mass, for the sub-Chandrasekhar models with  $Z = 0.0225$  and  $\xi_{\text{CO}} = 0.9$ .

The trends with progenitor metallicity of the yields of elements and isotopes in sub-Chandrasekhar models (Figs. 15 and 17) resemble those in Chandrasekhar models, discussed in Section 4.1, the main difference being that in subCh models the nickel isotopic yields are strongly metallicity dependent.

The WD mass in subCh models plays a role similar to that of the deflagration-to-detonation transition density in Chandra models, in the sense that it is the leading parameter determining the ejected mass of  $^{56}\text{Ni}$  and, hence, the luminosity of the supernova. Here (Fig. 16), as in Chandra models, the ratios of most elements with respect to iron decrease monotonously with increasing iron yield. However, there are two notable exceptions, cobalt and nickel, whose yields increase further than that of iron with increasing WD mass.

Most isotopes from chromium to nickel are produced in almost solar proportions in the normal luminosity models (Fig. 18). In contrast with Chandra models,  $^{50}\text{Ti}$ ,  $^{54}\text{Cr}$ , and

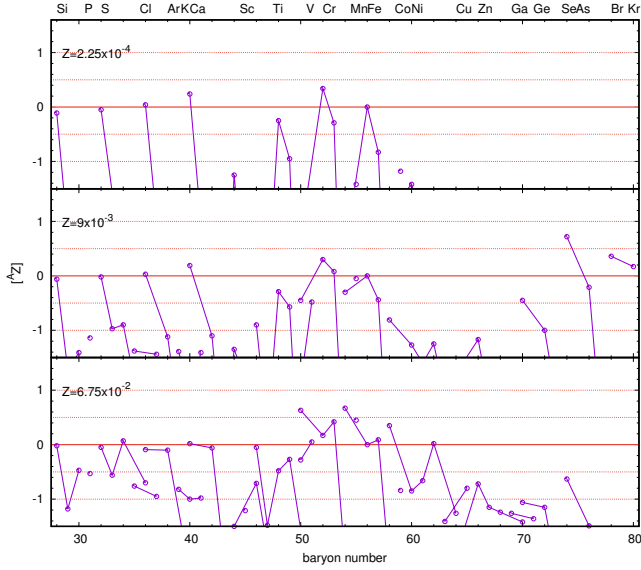


**Figure 17.** Variation of the isotopic yields with respect to metallicity, for the sub-Chandrasekhar models with  $M_{\text{WD}} = 0.97 M_{\odot}$  and  $\xi_{\text{CO}} = 0.9$ .

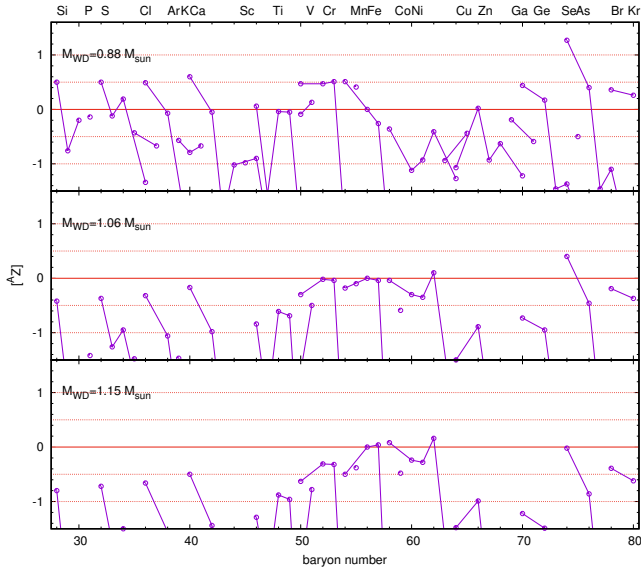


**Figure 18.** Variation of the isotopic yields with respect to the WD mass, for the sub-Chandrasekhar models with  $Z = 0.0225$  and  $\xi_{\text{CO}} = 0.9$ .

$^{58}\text{Fe}$  are underproduced in all models, which may help to compensate for their overproduction in Chandra models if both explosion scenarios contribute in similar proportions to SN Ia.

#### 4.3 Radioactivities

Tables 5 and 6 give the yields of the most abundant radioactive isotopes with half-life longer than one day. We have included all the isotopes whose yield in any one of the models presented in this work is larger than  $10^{-6} M_{\odot}$ .

Table 7 gives the maximum yield of these radioactive isotopes in all our models. The yields of typical targets of  $\gamma$ -ray observations of supernova remnants, e.g.  $^{26}\text{Al}$  and  $^{44}\text{Ti}$ , are pretty small, on the order of  $10^{-5} - 10^{-6} M_{\odot}$ , while other isotopes, e.g.  $^{59}\text{Ni}$ , are produced in interesting amounts.

## 5 CONCLUSIONS

We have computed the nucleosynthesis and hydrodynamics output for spherically symmetric models of SN Ia belonging to two explosion paradigms: the delayed-detonation of a Chandrasekhar-mass WD, and the pure central detonation of a sub-Chandrasekhar mass WD. Our models differ from existing compilations of SN Ia nucleosynthesis in two aspects. First, we have computed the nucleosynthesis using a large nuclear network of up to 722 nuclides in the hydrodynamics code, instead of post-processing the output. Second, we introduce the concept of SNR-calibrated SN Ia nucleosynthesis models.

Since our models are one-dimensional they cannot account for the effect of hydrodynamical instabilities and turbulence that are regularly found in multidimensional simulations of SN Ia (e.g. Plewa et al. 2004; Röpke et al. 2006; Bravo & García-Senz 2006; Kasen & Woosley 2007). In spite of these shortcomings, the results of many one-dimensional models compare well with observations of both SN Ia and their remnants (Höflich & Khokhlov 1996; Nugent et al. 1997; Badenes et al. 2006; Blondin et al. 2013; Hoefflich et al. 2017; Martínez-Rodríguez et al. 2018), many SN Ia show a high level of stratification, in better agreement with one-dimensional models than multidimensional ones (e.g. Tanaka et al. 2011b), and many remnants display geometries close to spherical symmetry (Lopez et al. 2011). However, the reader should be aware of the limitations of the one-dimensional hydrodynamical approach.

We have established that the combined variation of the rates in four key reactions involving  $^{12}\text{C}$  and  $^{16}\text{O}$  ( $^{12}\text{C}+^{16}\text{O}$ ,  $^{12}\text{C}+^{12}\text{C}$ ,  $^{16}\text{O}+^{16}\text{O}$ , and  $^{16}\text{O}+\gamma \rightarrow ^{12}\text{C}+\alpha$ ) within the uncertainties has the same effect than the suppression of the rate of the single reaction  $^{12}\text{C}+^{16}\text{O}$  by a factor  $\xi_{\text{CO}} = 0.9$ . For the sake of simplicity, we adopt this single change as representative of the changes that are needed to reconcile the nucleosynthetic yields of SN Ia models with the Ca/S and Ar/S mass ratios measured in Galactic and Magellanic Cloud Type Ia SNRs (Martínez-Rodríguez et al. 2017), and call this family of modified SN Ia models “SNR-calibrated SN Ia models”.

For all models, we have computed the hydrodynamics and nucleosynthesis starting from WDs with metallicities in the range from  $Z = 0.000225$  to  $Z = 0.0675$ . For Chandrasekhar-mass models we have computed explosions with deflagration-to-detonation transition densities ranging from  $1.2 \times 10^7 \text{ g cm}^{-3}$  to  $4.0 \times 10^7 \text{ g cm}^{-3}$ , while for sub-Chandrasekhar mass models we have allowed the mass of the exploding WD to vary between  $0.88 M_{\odot}$  and  $1.15 M_{\odot}$ . The explosions of Chandrasekhar-mass WDs with  $\rho_{\text{DDT}} = 2.4 \times 10^7 \text{ g cm}^{-3}$  and of sub-Chandrasekhar mass WDs with  $M_{\text{WD}} = 1.06 M_{\odot}$  should be representative of normal-luminosity SN Ia, since they produce between  $0.55 M_{\odot}$  and  $0.75 M_{\odot}$  of  $^{56}\text{Ni}$ .

There is a remarkable difference between



**Table 5.** Radioactivities with half-life longer than one day in Chandrasekhar-mass DDT models with  $\xi_{\text{CO}} = 0.9$ .

$\rho_{\text{DDT}}$	1.2E+07	1.2E+07	1.2E+07	1.2E+07	1.2E+07	1.6E+07	1.6E+07	1.6E+07	1.6E+07	1.6E+07
Z	2.25E-4	2.25E-3	9.00E-3	2.25E-2	6.75E-2	2.25E-4	2.25E-3	9.00E-3	2.25E-2	6.75E-2
Al26	1.07E-07	2.87E-07	3.99E-07	6.63E-07	1.18E-06	8.41E-08	1.48E-07	2.07E-07	3.31E-07	5.10E-07
P 32	1.97E-10	2.48E-08	1.36E-07	5.23E-07	4.89E-06	1.28E-10	1.66E-08	8.86E-08	3.28E-07	2.71E-06
P 33	8.11E-11	1.86E-08	1.26E-07	4.90E-07	3.81E-06	4.74E-11	1.11E-08	7.68E-08	3.00E-07	2.19E-06
S 35	2.46E-11	6.29E-09	7.54E-08	7.20E-07	1.11E-05	1.47E-11	4.07E-09	4.86E-08	4.48E-07	6.34E-06
Ar37	6.52E-06	1.17E-05	2.47E-05	4.01E-05	6.09E-05	4.55E-06	8.71E-06	1.78E-05	2.87E-05	4.48E-05
Ca41	9.76E-07	2.19E-06	5.51E-06	9.45E-06	1.31E-05	8.78E-07	1.77E-06	4.18E-06	6.92E-06	9.82E-06

Sample of Table 5, the full version is available online. The meaning of the columns is explained in the text.

**Table 6.** Radioactivities with half-life longer than one day in sub-Chandrasekhar models with  $\xi_{\text{CO}} = 0.9$ .

$M_{\text{WD}}$	0.88	0.88	0.88	0.88	0.88	0.97	0.97	0.97	0.97	0.97
Z	2.25E-4	2.25E-3	9.00E-3	2.25E-2	6.75E-2	2.25E-4	2.25E-3	9.00E-3	2.25E-2	6.75E-2
Al26	7.78E-08	2.03E-07	2.80E-07	4.27E-07	6.16E-07	4.06E-08	7.53E-08	1.02E-07	1.46E-07	1.92E-07
P 32	1.47E-10	1.96E-08	1.06E-07	3.82E-07	2.98E-06	7.04E-11	9.88E-09	4.99E-08	1.68E-07	1.18E-06
P 33	5.44E-11	1.46E-08	9.79E-08	3.61E-07	2.42E-06	2.68E-11	6.24E-09	4.03E-08	1.48E-07	9.83E-07
S 35	1.83E-11	4.98E-09	5.64E-08	4.94E-07	6.51E-06	8.28E-12	2.70E-09	2.88E-08	2.30E-07	2.77E-06
Ar37	5.63E-06	9.53E-06	1.93E-05	2.97E-05	4.42E-05	4.24E-06	7.82E-06	1.46E-05	2.29E-05	3.47E-05
Ca41	8.23E-07	1.88E-06	4.49E-06	7.07E-06	9.58E-06	9.39E-07	1.79E-06	3.61E-06	5.71E-06	7.96E-06

Sample of Table 6, the full version is available online. The meaning of the columns is explained in the text.

**Table 7.** Maximum yield, in solar masses, of the radioactive isotopes in all our models.

Al26	$1.7 \times 10^{-6}$	Mn54	$1.2 \times 10^{-5}$
P 32	$4.9 \times 10^{-6}$	Fe55	$2.0 \times 10^{-2}$
P 33	$3.8 \times 10^{-6}$	Fe59	$1.2 \times 10^{-5}$
S 35	$1.1 \times 10^{-5}$	Fe60	$1.4 \times 10^{-4}$
Ar37	$6.5 \times 10^{-5}$	Co56	$1.7 \times 10^{-4}$
Ca41	$1.3 \times 10^{-5}$	Co57	$8.4 \times 10^{-4}$
Ti44	$5.1 \times 10^{-5}$	Co58	$4.8 \times 10^{-6}$
V 48	$6.8 \times 10^{-4}$	Co60	$7.4 \times 10^{-6}$
V 49	$4.0 \times 10^{-5}$	Ni56	$9.3 \times 10^{-1}$
Cr51	$1.8 \times 10^{-4}$	Ni57	$3.4 \times 10^{-2}$
Mn52	$1.6 \times 10^{-2}$	Ni59	$1.6 \times 10^{-3}$
Mn53	$2.2 \times 10^{-3}$	Zn65	$2.7 \times 10^{-6}$

Chandrasekhar-mass and sub-Chandrasekhar mass models. In the first ones, the increment in the IGE yields with  $\rho_{\text{DDT}}$  comes predominantly in the form of iron. In the second ones, this increment of IGE with  $M_{\text{WD}}$  is contributed significantly by cobalt and nickel. We also note that the even-atomic number IMEs are overproduced with respect to iron in the models that produce the less  $^{56}\text{Ni}$  (hence, the most sub-luminous ones), for all WD masses.

The neutron-rich isotopes  $^{50}\text{Ti}$ ,  $^{54}\text{Cr}$ , and  $^{58}\text{Fe}$  are overproduced with respect to  $^{56}\text{Fe}$  in the Chandrasekhar-mass models because of the high initial central density. On the other hand, the same isotopes are underproduced in all sub-Chandrasekhar mass models, so a combination of explosions of all masses might be able to produce the proportions of these isotopes in the Solar System.

We notice an important production of the isotopes  $^{74,76}\text{Se}$  and  $^{78,80}\text{Kr}$ , which are subdominant with respect to the selenium and krypton isotopic composition in the Solar System. All these isotopes are less neutron-rich than the most abundant ones in the Solar System, and are produced in the outermost shells of the exploding WD.

Future X-ray facilities like *XRISM* and *Athena* may be able to discriminate models with respect to the rates of the

aforementioned four reactions involving carbon and oxygen. In this respect, the mass ratio of potassium to calcium looks as the most promising observational target, although this point is in need of further investigation. One possible strategy would be to fix the properties of the ISM and, if unknown, the age of observed supernova remnants through the most prominent lines in the SNR X-ray spectra and, as well, fix the best explosion model describing the spectra. Thereafter, the mass ratio K/Ca would provide the best estimate of the involved reaction rates, since the yield of K is sensitive to their values. The results would have to be cross-checked for as many SNRs as possible, in order to provide a statistically convincing constraint on the relevant nuclear physics.

## ACKNOWLEDGEMENTS

We thank the anonymous referee for a very detailed and constructive report, which has contributed to improve the presentation of this work. E.B. acknowledges funding from the MINECO-FEDER grant AYA2015-63588-P; H.M.-R. acknowledges support from NASA ADAP grant NNX15AM03G S01, a PITT PACC, and a Zacheus Daniel Predoctoral Fellowship. E.B. wishes to dedicate this work to the loving memory of Wilma.

## REFERENCES

- Ashall C., Mazzali P. A., Pian E., James P. A., 2016, *MNRAS*, **463**, 1891
- Badenes C., Borkowski K. J., Hughes J. P., Hwang U., Bravo E., 2006, *ApJ*, **645**, 1373
- Badenes C., Bravo E., Hughes J. P., 2008, *ApJ*, **680**, L33
- Blinnikov S. I., Dunina-Barkovskaya N. V., Nadyozhin D. K., 1996, *ApJS*, **106**, 171
- Blondin S., Dessart L., Hillier D. J., Khokhlov A. M., 2013, *MNRAS*, **429**, 2127
- Blondin S., Dessart L., Hillier D. J., Khokhlov A. M., 2017, *MNRAS*, **470**, 157

- Botyánszki J., Kasen D., 2017, *ApJ*, **845**, 176
- Branch D., Patchett B., 1973, *MNRAS*, **161**, 71
- Branch D., Baron E., Hall N., Melakayil M., Parrent J., 2005, *PASP*, **117**, 545
- Bravo E., García-Senz D., 1999, *MNRAS*, **307**, 984
- Bravo E., García-Senz D., 2006, *ApJ*, **642**, L157
- Bravo E., Martínez-Pinedo G., 2012, *Phys. Rev. C*, **85**, 055805
- Bravo E., Domínguez I., Badenes C., Piersanti L., Straniero O., 2010, *ApJ*, **711**, L66
- Buchmann L., 1996, *ApJ*, **468**, L127+
- Cardillo M., Amato E., Blasi P., 2016, *A&A*, **595**, A58
- Caughlan G. R., Fowler W. A., 1988, *Atomic Data and Nuclear Data Tables*, **40**, 283
- Caughlan G. R., Fowler W. A., Harris M. J., Zimmerman B. A., 1985, *Atomic Data and Nuclear Data Tables*, **32**, 197
- Chevalier R. A., 1977, *ARA&A*, **15**, 175
- Colella P., Glaz H. M., 1985, *Journal of Computational Physics*, **59**, 264
- Colella P., Woodward P. R., 1984, *Journal of Computational Physics*, **54**, 174
- Cyburt R. H., et al., 2010, *ApJS*, **189**, 240
- Dave P., Kashyap R., Fisher R., Timmes F., Townsley D., Byrohl C., 2017, *ApJ*, **841**, 58
- Diamond T. R., Hoefflich P., Gerardy C. L., 2015, *ApJ*, **806**, 107
- Dimitriadis G., et al., 2017, *MNRAS*, **468**, 3798
- Dunkley S. D., Sharpe G. J., Falle S. A. E. G., 2013, *MNRAS*, **431**, 3429
- Fink M., Röpke F. K., Hillebrandt W., Seitenzahl I. R., Sim S. A., Kromer M., 2010, *A&A*, **514**, A53+
- Fuller G. M., Fowler W. A., Newman M. J., 1982, *ApJS*, **48**, 279
- Gamezo V. N., Wheeler J. C., Khokhlov A. M., Oran E. S., 1999, *ApJ*, **512**, 827
- Gerardy C. L., et al., 2007, *ApJ*, **661**, 995
- Graur O., et al., 2018, *ApJ*, **859**, 79
- Grevesse N., Noels A., 1993, in Prantzos N., Vangioni-Flam E., Casse M., eds, *Origin and Evolution of the Elements*. pp 15–25
- Hitomi Collaboration et al., 2018, *PASJ*, **70**, 16
- Hoefflich P., Wheeler J. C., Thielemann F. K., 1998, *ApJ*, **495**, 617
- Hoefflich P., et al., 2017, preprint, ([arXiv:1707.05350](https://arxiv.org/abs/1707.05350))
- Höflich P., Khokhlov A., 1996, *ApJ*, **457**, 500
- Kasen D., Woosley S. E., 2007, *ApJ*, **656**, 661
- Kasen D., Röpke F. K., Woosley S. E., 2009, *Nature*, **460**, 869
- Katsuma M., 2012, *ApJ*, **745**, 192
- Khokhlov A. M., 1991, *A&A*, **245**, 114
- Leung S.-C., Nomoto K., 2017, preprint, ([arXiv:1710.04254](https://arxiv.org/abs/1710.04254))
- Lopez L. A., Ramirez-Ruiz E., Huppenkothen D., Badenes C., Pooley D. A., 2011, *ApJ*, **732**, 114
- Maguire K., et al., 2018, *MNRAS*, **477**, 3567
- Maoz D., Graur O., 2017, *ApJ*, **848**, 25
- Martínez-Pinedo G., Langanke K., Dean D. J., 2000, *ApJS*, **126**, 493
- Martínez-Rodríguez H., Piro A. L., Schwab J., Badenes C., 2016, *ApJ*, **825**, 57
- Martínez-Rodríguez H., et al., 2017, *ApJ*, **843**, 35
- Martínez-Rodríguez H., et al., 2018, *ApJ*, **865**, 151
- Matteucci F., Tornambe A., 1987, *A&A*, **185**, 51
- Matteucci F., Spitoni E., Recchi S., Valiante R., 2009, *A&A*, **501**, 531
- Mazzali P. A., Sauer D. N., Pastorello A., Benetti S., Hillebrandt W., 2008, *MNRAS*, **386**, 1897
- McWilliam A., Piro A. L., Badenes C., Bravo E., 2018, *ApJ*, **857**, 97
- Miles B. J., Townsley D. M., Shen K. J., Timmes F. X., Moore K., 2018, preprint, ([arXiv:1806.07820](https://arxiv.org/abs/1806.07820))
- Minkowski R., 1939, *ApJ*, **89**, 156
- Minkowski R., 1941, *PASP*, **53**, 224
- Nandra K., et al., 2013, preprint, ([arXiv:1306.2307](https://arxiv.org/abs/1306.2307))
- Nomoto K., 1984, *ApJ*, **277**, 791
- Nomoto K., Thielemann F.-K., Yokoi K., 1984, *ApJ*, **286**, 644
- Nugent P., Baron E., Branch D., Fisher A., Hauschildt P. H., 1997, *ApJ*, **485**, 812
- Oda T., Hino M., Muto K., Takahara M., Sato K., 1994, *Atomic Data and Nuclear Data Tables*, **56**, 231
- Ogata S., Ichimaru S., 1987, *Phys. Rev. A*, **36**, 5451
- Park S., et al., 2013, *ApJ*, **767**, L10
- Perlmutter S., et al., 1999, *ApJ*, **517**, 565
- Piersanti L., Bravo E., Cristallo S., Domínguez I., Straniero O., Tornambé A., Martínez-Pinedo G., 2017, *ApJ*, **836**, L9
- Plewa T., Calder A. C., Lamb D. Q., 2004, *ApJ*, **612**, L37
- Prantzos N., Abia C., Limongi M., Chieffi A., Cristallo S., 2018, *MNRAS*, **476**, 3432
- Pruet J., Fuller G. M., 2003, *ApJS*, **149**, 189
- Pskovskii Y. P., 1969, *Soviet Ast.*, **12**, 750
- Rauscher T., Heger A., Hoffman R. D., Woosley S. E., 2002, *ApJ*, **576**, 323
- Riess A. G., et al., 1998, *AJ*, **116**, 1009
- Riess A. G., et al., 2004, *ApJ*, **607**, 665
- Röpke F. K., Hillebrandt W., Niemeyer J. C., Woosley S. E., 2006, *A&A*, **448**, 1
- Sasdeli M., Mazzali P. A., Pian E., Nomoto K., Hachinger S., Cappellaro E., Benetti S., 2014, *MNRAS*, **445**, 711
- Sawala T., Scannapieco C., Maio U., White S., 2010, *MNRAS*, **402**, 1599
- Schwab J., Martínez-Rodríguez H., Piro A. L., Badenes C., 2017, *ApJ*, **851**, 105
- Scolnic D. M., et al., 2018, *ApJ*, **859**, 101
- Seitenzahl I. R., Townsley D. M., Peng F., Truran J. W., 2009, *Atomic Data and Nuclear Data Tables*, **95**, 96
- Sharpe G. J., 2001, *MNRAS*, **322**, 614
- Shen K. J., Kasen D., Miles B. J., Townsley D. M., 2018, *ApJ*, **854**, 52
- Sim S. A., Röpke F. K., Hillebrandt W., Kromer M., Pakmor R., Fink M., Ruiter A. J., Seitenzahl I. R., 2010, *ApJ*, **714**, L52
- Sinitsyna V. G., Sinitsyna V. Y., 2011, *Astronomy Letters*, **37**, 621
- Stehle M., Mazzali P. A., Benetti S., Hillebrandt W., 2005, *MNRAS*, **360**, 1231
- Takamoto M., Kirk J. G., 2015, *ApJ*, **809**, 29
- Tanaka M., Mazzali P. A., Stanishev V., Maurer I., Kerzendorf W. E., Nomoto K., 2011a, *MNRAS*, **410**, 1725
- Tanaka M., Mazzali P. A., Stanishev V., Maurer I., Kerzendorf W. E., Nomoto K., 2011b, *MNRAS*, **410**, 1725
- Tashiro M., et al., 2018, in *Society of Photo-Optical Instrumentation Engineers (SPIE) Conference Series*. p. 10699, doi:10.1117/12.2309455
- Thielemann F.-K., Nomoto K., Yokoi K., 1986, *A&A*, **158**, 17
- Timmes F. X., Brown E. F., Truran J. W., 2003, *ApJ*, **590**, L83
- Townsley D. M., Miles B. J., Timmes F. X., Calder A. C., Brown E. F., 2016, *ApJS*, **225**, 3
- Warren J. S., et al., 2005, *ApJ*, **634**, 376
- Wheeler J. C., Harkness R. P., 1986, in Madore B. F., Tully R. B., eds, *NATO Advanced Science Institutes (ASI) Series C Vol. 180, NATO Advanced Science Institutes (ASI) Series C*. pp 45–54
- Wood-Vasey W. M., et al., 2007, *ApJ*, **666**, 694
- Woosley S. E., Kasen D., 2010, preprint, ([arXiv:1010.5292](https://arxiv.org/abs/1010.5292))
- Woosley S. E., Weaver T. A., 1994, *ApJ*, **423**, 371
- Woosley S. E., Arnett W. D., Clayton D. D., 1971, *Physical Review Letters*, **27**, 213
- Woosley S. E., Kasen D., Blinnikov S., Sorokina E., 2007, *ApJ*, **662**, 487
- Xu Y., Takahashi K., Goriely S., Arnould M., Ohta M., Utsumomiya H., 2013, *Nuclear Physics A*, **918**, 61
- Yakovlev D. G., Shalybkov D. A., 1989, *Astrophysics and Space Physics Reviews*, **7**, 311

Yamaguchi H., et al., 2015, *ApJ*, **801**, L31  
 Yang X. J., Tsunemi H., Lu F. J., Li A., Xiang F. Y., Xiao H. P.,  
 Zhong J. X., 2013, *ApJ*, **766**, 44  
 deBoer R. J., et al., 2017, *Reviews of Modern Physics*, **89**, 035007

## APPENDIX A: YIELDS OF MODELS WITH THE STANDARD $^{12}\text{C}+^{16}\text{O}$ REACTION RATE

In this Section, we give the final (after radioactive decays) elemental and isotopic yields of the SN Ia models that use the standard set of reaction rates,  $^{12}\text{C}+^{16}\text{O}$  included (Tables A1 and A2). We give as well the yields of the most abundant radioactive isotopes with half-life longer than one day (Tables A3 and A4).

## APPENDIX B: HYDRODYNAMICS AND NUCLEOSYNTHESIS CODE

The supernova code solves the hydrodynamics and nucleosynthesis along the explosion in a single run, i.e. with no postprocessing of the nuclear equations. This approach has the advantage that the binding energy released in the nuclear processes is treated self-consistently in the hydro part of the problem, as well as the dependence of the equation of state on the chemical composition. As an example, during alpha-rich freeze-out from nuclear statistical equilibrium (NSE) the specific nuclear binding energy can change as much as  $9 \times 10^{16} \text{ erg g}^{-1}$  ( $\sim 10\%$ ), while the mean molar weight varies from  $\sim 30 - 32$  at the beginning of the freeze-out up to  $\sim 52 - 54$  at the end of the same period.

The hydrodynamic solver is explicit and based on the piecewise-parabolich method (PPM) in the Lagrangian version of Colella & Woodward (1984), with spherical symmetry and gravity. We adopt the modifications introduced in Colella & Glaz (1985) to solve the Riemann problem with a general equation of state (EOS). The integration of the hydrodynamic equations with the PPM scheme is followed by the integration of the nuclear kinetic equations, and then the temperature is updated according to the nuclear energy released (and to the energy loss rate due to neutrinos generated in weak transitions). We take profit of the flattening algorithms introduced by Colella & Woodward (1984), in order to identify the mass shells affected by shocks during the detonation phase of the SN Ia explosion, and we forbid nuclear burning until the shock has passed away from the shell. This procedure mimicks the expected behaviour of actual detonations, in which the dissipation associated with the leading shock front heats matter almost instantaneously to temperatures on the order of  $3 - 4 \times 10^9 \text{ K}$  (depending on the fuel density), with no change in the chemical composition.

Our EOS accounts for radiation and for fully ionized matter: electrons and positrons (Blinnikov et al. 1996), relativistic and non-relativistic with arbitrary degree of degeneracy, and ions, with Coulomb and polarization corrections from Yakovlev & Shalybkov (1989) and Ogata & Ichimaru (1987), see also Bravo & García-Senz (1999). The information about the chemical composition is fully shared between the nuclear solver and the hydro solver. It has an imprint, for instance, in the Coulomb corrections to the ionic EOS.

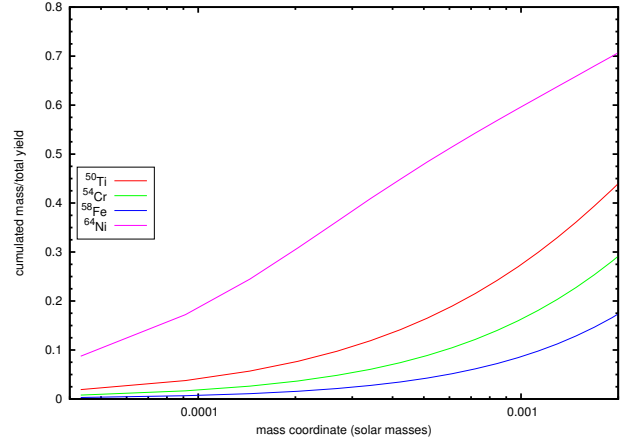


**Figure B1.** Final abundance profile of several neutronized isotopes close to the center of the WD in model ddt2p4\_Z9e-3-ξCO0p9. The ordinate gives the integrated mass, starting from the center, normalized by the total yield of the isotope. It shows that the adopted spatial resolution is fine enough to smoothly represent the production of  $^{50}\text{Ti}$ ,  $^{54}\text{Cr}$ , and  $^{58}\text{Fe}$ . The central layer contributes slightly less than 10% to the total mass of  $^{64}\text{Ni}$ , which is anyway underproduced in this model by a factor  $\geq 2$  (see, e.g., Fig. 13).

Within a thermonuclear supernova explosion, matter changes from a state of extreme degeneracy to partial and weak degeneracy. We integrate a temperature,  $T$ , equation whenever matter is strongly degenerate, and a specific energy,  $e$ , equation otherwise. In practice, the first option is chosen when

$$\left| \frac{(\partial e / \partial \log T)}{(\partial e / \partial \log \rho)} \right| < 0.01. \quad (\text{B1})$$

### B1 Spacing and time steps

The shell spacing, in terms of Lagrangian mass coordinate, is uniform and equal to  $0.002 \times M_{\text{WD}}$  in all the star but for the innermost and outermost  $0.02 \times M_{\text{WD}}$ , where it is finer. Starting from a central mass shell of  $3 \times 10^{-5} \times M_{\text{WD}}$ , the mass of each shell increases by 10% until reaching the width of  $0.002 \times M_{\text{WD}}$ . In the outermost layers, we apply the same procedure as in the center but in reverse order. In total, there are 562 mass shells in each model. Figure B1 shows the final abundance profile of the isotopes that are most contributed by the central layers in a delayed-detonation model, where it can be seen that their production is well resolved by the adopted spatial zoning. The fine zoning applied in the outer layers contributes to reproducing accurately the density gradient and the curvature effect on the propagation of the detonation front (Sharpe 2001; Dunkley et al. 2013; Miles et al. 2018). As an example, at the time of formation of the detonation in model ddt2p4\_Z9e-3\_std, the spatial resolution is better than  $\Delta R/R < 1\%$  in all the WD, and the relative change in density between adjacent fuel layers is less than  $\Delta \rho / \rho < 10\%$  in all but the outermost  $10^{-4} M_{\odot}$ .

The time step is adaptive to ensure that the integration variables do not change too much in a single time step. The variables we control are density, temperature, velocity,

**Table A1.** Nucleosynthesis in Chandrasekhar-mass DDT models with standard  $^{12}\text{C}+^{16}\text{O}$  reaction rate.

$\rho_{\text{DDT}}$		1.2E+07	1.2E+07	1.2E+07	1.2E+07	1.2E+07	1.6E+07	1.6E+07	1.6E+07	1.6E+07	1.6E+07
$Z$		2.25E-4	2.25E-3	9.00E-3	2.25E-2	6.75E-2	2.25E-4	2.25E-3	9.00E-3	2.25E-2	6.75E-2
elem	2He	1.31E-04	1.22E-04	1.00E-04	4.64E-05	3.05E-08	1.32E-04	1.23E-04	1.01E-04	4.63E-05	3.18E-08
isot	2He3	1.80E-12	1.78E-12	1.76E-12	1.62E-12	1.33E-12	1.80E-12	1.78E-12	1.76E-12	1.62E-12	1.33E-12
isot	2He4	1.31E-04	1.22E-04	1.00E-04	4.64E-05	3.05E-08	1.32E-04	1.23E-04	1.01E-04	4.62E-05	3.18E-08
elem	6C	5.02E-03	4.94E-03	4.85E-03	5.16E-03	5.19E-03	2.40E-03	2.37E-03	2.55E-03	2.50E-03	2.40E-03
isot	6C12	5.02E-03	4.94E-03	4.85E-03	5.16E-03	5.19E-03	2.40E-03	2.37E-03	2.55E-03	2.50E-03	2.40E-03
isot	6C13	2.08E-10	3.58E-09	1.25E-08	3.02E-08	7.54E-08	1.06E-10	1.58E-09	6.48E-09	1.52E-08	3.90E-08

Sample of Table A1, the full version is available online. The meaning of the columns is the same as in Table 3.

**Table A2.** Nucleosynthesis in sub-Chandrasekhar models with standard  $^{12}\text{C}+^{16}\text{O}$  reaction rate.

$M_{\text{WD}}$		0.88	0.88	0.88	0.88	0.88	0.97	0.97	0.97	0.97	0.97
$Z$		2.25E-4	2.25E-3	9.00E-3	2.25E-2	6.75E-2	2.25E-4	2.25E-3	9.00E-3	2.25E-2	6.75E-2
elem	2He	9.87E-08	9.71E-08	7.65E-08	3.33E-08	2.92E-10	2.25E-04	2.39E-04	2.72E-04	3.35E-04	4.93E-04
isot	2He3	1.97E-16	1.97E-16	1.99E-16	2.04E-16	2.39E-16	7.16E-16	7.09E-16	6.89E-16	6.52E-16	5.39E-16
isot	2He4	9.87E-08	9.71E-08	7.65E-08	3.33E-08	2.92E-10	2.25E-04	2.39E-04	2.72E-04	3.35E-04	4.93E-04
elem	6C	4.10E-03	4.08E-03	3.99E-03	3.83E-03	3.33E-03	1.67E-03	1.66E-03	1.63E-03	1.56E-03	1.36E-03
isot	6C12	4.10E-03	4.08E-03	3.99E-03	3.83E-03	3.33E-03	1.67E-03	1.66E-03	1.62E-03	1.55E-03	1.36E-03
isot	6C13	2.25E-10	3.71E-09	1.23E-08	2.61E-08	5.62E-08	9.58E-11	1.53E-09	5.68E-09	1.28E-08	2.83E-08

Sample of Table A2, the full version is available online. The meaning of the columns is the same as in Table 3.

**Table A3.** Radioactivities with half-life longer than one day in Chandrasekhar-mass models with the standard  $^{12}\text{C}+^{16}\text{O}$  reaction rate.

$\rho_{\text{DDT}}$		1.2E+07	1.2E+07	1.2E+07	1.2E+07	1.2E+07	1.6E+07	1.6E+07	1.6E+07	1.6E+07	1.6E+07
$Z$		2.25E-4	2.25E-3	9.00E-3	2.25E-2	6.75E-2	2.25E-4	2.25E-3	9.00E-3	2.25E-2	6.75E-2
Al26		1.29E-07	3.89E-07	5.25E-07	8.19E-07	1.32E-06	8.06E-08	2.01E-07	2.86E-07	3.97E-07	5.71E-07
P 32		2.25E-10	2.97E-08	1.57E-07	5.68E-07	4.76E-06	1.40E-10	2.00E-08	1.05E-07	3.41E-07	2.57E-06
P 33		8.13E-11	2.34E-08	1.49E-07	5.37E-07	3.73E-06	5.02E-11	1.38E-08	9.17E-08	3.13E-07	2.10E-06
S 35		2.74E-11	6.40E-09	7.57E-08	7.14E-07	1.08E-05	1.58E-11	4.10E-09	4.96E-08	4.22E-07	5.93E-06
Ar37		6.31E-06	1.08E-05	2.22E-05	3.74E-05	6.53E-05	4.11E-06	7.87E-06	1.65E-05	2.73E-05	4.77E-05
Ca41		6.71E-07	1.72E-06	4.13E-06	7.20E-06	1.08E-05	5.64E-07	1.35E-06	3.19E-06	5.38E-06	7.94E-06

Sample of Table A3, the full version is available online. The meaning of the columns is the same as in Table 5.

abundances, and shell sound crossing time (Courant condition). The time step in the hydrodynamic solver,  $\Delta t$ , can be different from that of the nuclear network solver,  $\Delta t_{\text{nuc}}$ . Besides, the value of  $\Delta t$  is common to all mass shells at any given integration step, while the value of  $\Delta t_{\text{nuc}}$  can differ from shell to shell. Specifically, we require for each hydrodynamic time step, that the relative change is smaller than 0.1% in density, 0.2% in temperature, and 20% in velocity (with a floor of  $10^6 \text{ cm s}^{-1}$ ). With respect to the nuclear network time step, we accept a relative change up to 2% in the abundance of any nuclear species whose molar abundance is larger than  $10^{-6} \text{ mol g}^{-1}$  in any mass shell. If the new time step results smaller than 40% of the previous one, the integration of the last time step, either a hydrodynamic or a nuclear one, is rejected and repeated with a smaller time step, until the above condition is fulfilled. The repetition of a hydrodynamic integration step implies that of the nuclear solver for all mass shells. On the other hand, the repetition of a nuclear integration step does not require that of the hydrodynamic solution.

When the nuclear time step is smaller than the current hydrodynamic time step, the nuclear evolution is solved with frozen temperature and density until the accumulated nuclear time equals the hydrodynamic time step. After accounting for the nuclear energy released, sometimes the condition of maximum relative change for the temperature is not

fulfilled, in which case the whole process is repeated starting from the last hydro and nuclear good values, but with a smaller  $\Delta t$ . In Fig. B2, there can be seen an example of the run of the hydrodynamic time step along the explosion.

## B2 Nuclear network

The nuclear network, shown in Fig. B3, is the same as in [Bravo & Martínez-Pinedo \(2012\)](#). The network extends to sufficiently neutron-rich isotopes, beyond the valley of beta stability, to describe the high-density combustion phases, in which electron captures increase the mean neutron excess of matter to  $\sim 0.1$  (electron mole number,  $Y_e \sim 0.44$ ). The nuclear kinetic equations follow the time evolution of the mass fraction,  $X_i$ , of each species due to weak and strong interactions, including photodisintegrations and four fusion reactions ( $3\alpha$ ,  $^{12}\text{C}+^{12}\text{C}$ ,  $^{12}\text{C}+^{16}\text{O}$ , and  $^{16}\text{O}+^{16}\text{O}$ ), until the temperature falls below  $10^8 \text{ K}$ , after which time only the weak interactions are accounted for.

The nuclear network solver is implicit, iterative, and uses adaptive time steps. In each time step, the iterative procedure ends when the molar abundances of all nuclei with  $Y_i > 10^{-17} \text{ mol g}^{-1}$  have converged to better than  $10^{-4} \times \max(Y_i, 10^{-6} \text{ mol g}^{-1})$ .

The size and composition of the nuclear network changes each time step and may be different from mass shell



**Table A4.** Radioactivities with half-life longer than one day in sub-Chandrasekhar models with the standard  $^{12}\text{C}+^{16}\text{O}$  reaction rate.

$M_{\text{WD}}$	0.88	0.88	0.88	0.88	0.88	0.97	0.97	0.97	0.97	0.97
$Z$	2.25E-4	2.25E-3	9.00E-3	2.25E-2	6.75E-2	2.25E-4	2.25E-3	9.00E-3	2.25E-2	6.75E-2
Al26	9.89E-08	2.81E-07	3.74E-07	5.25E-07	7.03E-07	5.46E-08	1.07E-07	1.40E-07	1.87E-07	2.30E-07
P 32	1.68E-10	2.37E-08	1.23E-07	4.09E-07	2.91E-06	8.68E-11	1.24E-08	5.96E-08	1.84E-07	1.17E-06
P 33	5.59E-11	1.87E-08	1.16E-07	3.90E-07	2.38E-06	2.93E-11	8.08E-09	4.81E-08	1.62E-07	9.77E-07
S 35	1.93E-11	5.13E-09	5.74E-08	4.85E-07	6.31E-06	8.90E-12	2.83E-09	2.96E-08	2.27E-07	2.68E-06
Ar37	4.82E-06	8.15E-06	1.69E-05	2.76E-05	4.56E-05	3.37E-06	6.63E-06	1.32E-05	2.16E-05	3.59E-05
Ca41	4.95E-07	1.31E-06	3.16E-06	5.30E-06	7.52E-06	5.09E-07	1.19E-06	2.62E-06	4.35E-06	6.19E-06

Sample of Table A4, the full version is available online. The meaning of the columns is the same as in Table 5.

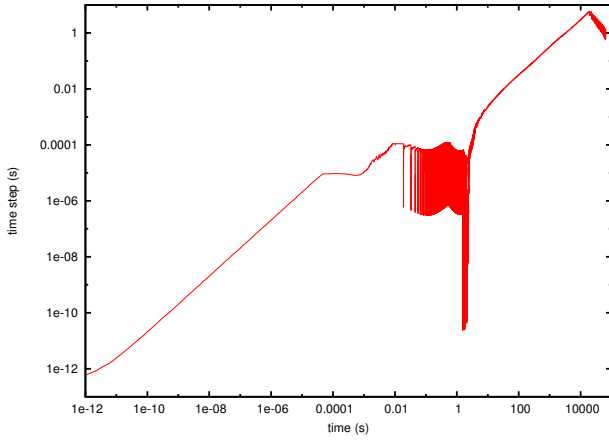


**Figure B2.** Hydrodynamic time step along the explosion of model ddt2p4\_Z9e-3\_std. The sudden decreases on the time step down to  $\Delta t \sim 10^{-7}$  s from time  $\sim 0.02$  s to  $\sim 1.5$  s belong to the arrival of the deflagration front to a new mass shell when the fuel density is high enough to assume a NSE state will be reached. In our models, the minimum fuel density at which NSE is forced is  $8 \times 10^7 \text{ g cm}^{-3}$ . Thereafter, the more pronounced decreases on the time step down to  $\Delta t \sim 10^{-11}$  s reflect the arrival of either the flame front or the detonation wave (through shock heating) to a new mass shell, and the subsequent acceleration of the nuclear reactions.

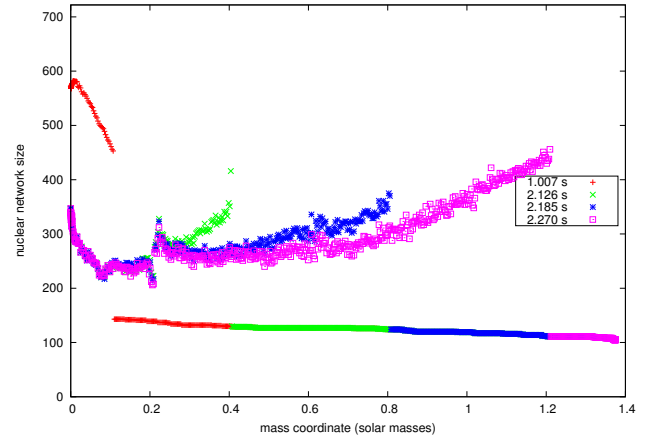


**Figure B4.** Number of nuclei actually present in the computational network as function of the Lagrangian mass coordinate in model ddt2p4\_Z9e-3\_std at four different times. At 1.007 s the explosion is still in the deflagration phase and registers the largest network size close to the center, where matter is in the NSE state. The other three times depicted, 2.126 s, 2.185 s and 2.270 s, belong to the detonation phase and show increasing network size close to the detonation front, and close to the WD surface as well. In each shell, the network size remains constant, on the order of 100 – 150 species, until the flame front reaches it, which results in overlapping of the different symbols at the plot bottom.

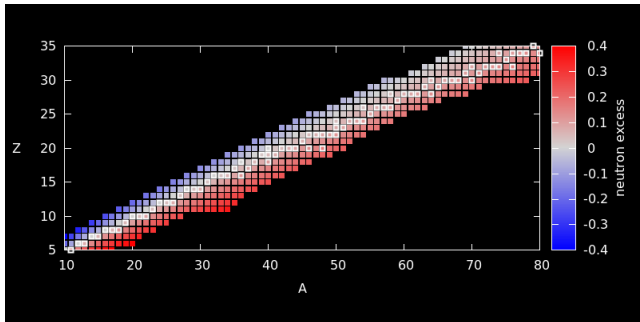


**Figure B3.** Nuclear network used in the hydrodynamic calculations reported in this paper. Location of the main contributors to nucleosynthesis, besides p, n, and  $\alpha$ , on the charge – baryon number plane, coloured according to their neutron excess (the actual network is slightly larger, from  $Z = 0$  to  $Z = 50$  and from  $A = 1$  to  $A = 100$ ). We highlighted the stable isotopes with an open white square.

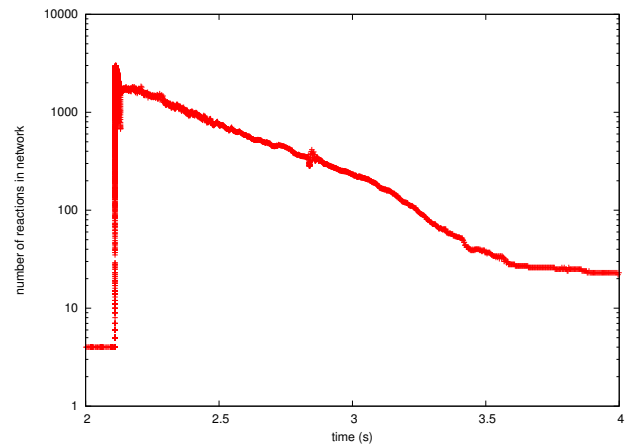


**Figure B5.** Time evolution of the number of nuclear reactions (strong and weak, including photodisintegrations and fusion reactions) in the network for the mass shell with Lagrangian mass coordinate  $0.3 M_{\odot}$  in model ddt2p4\_Z9e-3\_std.

to mass shell (see Fig. B4), with a maximum of 722 nuclides. The nuclides actually present in the network are determined according to the chemical abundances and the possible nuclear links to other abundant nuclei. Initially, the network is defined by neutrons and the rest of isotopes present in the Solar System mixture up to  $^{101}\text{In}$ . Thereafter, the network is formed by neutrons, protons, alphas, and those species with abundance  $Y_i > Y_{\text{thresh}} = 10^{-19} \text{ mol g}^{-1}$ , plus the nuclei that can be reached from any of the nuclei with  $Y_i > 100 \times Y_{\text{thresh}}$  by any one of the reactions included in the network. A reaction rate is included in the network only if the predicted change of a molar abundance in the next time step,  $\Delta t_{\text{nuc}}$ , is larger than a given threshold:

$$N_A \rho \langle \sigma v \rangle Y_i Y_j \Delta t_{\text{nuc}} > R_{\text{thresh}} = 10^{-13} \text{ mol g}^{-1}. \quad (\text{B2})$$

We show in Fig. B5 how the number of reactions in the network changes along the explosion for a typical mass shell. A similar method of integration of the nuclear evolutionary equations using an adaptive network has been described in [Rauscher et al. \(2002\)](#) and [Bravo & Martínez-Pinedo \(2012\)](#), the main novelty here is that it is solved along with the hydrodynamic evolution of the exploding WD.

### B3 Convergence of the nucleosynthesis calculation

In Table B1, we show the convergence of the nucleosynthesis results for model ddt2p4\_Z9e-3.std with respect to the chosen threshold values,  $Y_{\text{thresh}}$  and  $R_{\text{thresh}}$ , when any one of them is a factor ten smaller than our reference values,  $Y_{\text{thresh}} = 10^{-19} \text{ mol g}^{-1}$  and  $R_{\text{thresh}} = 10^{-13} \text{ mol g}^{-1}$ , while all other parameters are held constant. For either an abundance threshold or a reaction rate threshold an order of magnitude smaller than our reference values, the final kinetic energy changes by less than 0.09%, and the mass of  $^{56}\text{Ni}$  synthesized by less than 0.02%. Concerning the yields of the different nuclides, with respect to the modification of  $Y_{\text{thresh}}$  by a factor ten, the yields change by at most 0.001% for 33% of all nuclei and for 67% of nuclei with a mass yield,  $M_i$ , larger than  $10^{-3} M_{\odot}$ , while no nuclei with  $M_i > 10^{-3} M_{\odot}$  changes by more than 0.07%, no nuclei with  $M_i > 10^{-6} M_{\odot}$  changes by more than 2.7% ( $^{61}\text{Ni}$  is the one with the largest variation), and no nuclei with  $10^{-6} M_{\odot} > M_i > 10^{-12} M_{\odot}$  changes by more than 2.2% ( $^{47}\text{Ti}$ ). The records are similar although slightly worse when we consider the modification of  $R_{\text{thresh}}$  by a factor of ten. In this case, the largest variation belongs to  $^{47}\text{Ti}$ , whose mass yield is  $\sim 10^{-7} M_{\odot}$ .

### B4 Treatment of matter in NSE

At temperatures in excess of  $\sim 5 - 6 \times 10^9 \text{ K}$  and sufficiently high densities, most direct and reverse strong interactions achieve equilibrium, the NSE state, and the composition is determined by a Saha equation accounting for the nuclear mass, the nuclear partition function, density, temperature, and electron mole number. In our code, we assume matter achieves NSE when the burning front arrives to a mass shell with density  $\rho \geq \rho_{\text{NSE0}} = 8 \times 10^7 \text{ g cm}^{-3}$ . Below this density, we require a minimum temperature of  $T \geq T_{\text{NSE1}} = 5.5 \times 10^9 \text{ K}$  if density is  $\rho \geq \rho_{\text{NSE1}} = 2 \times 10^7 \text{ g cm}^{-3}$ , or  $T \geq T_{\text{NSE2}} = 6 \times 10^9 \text{ K}$  otherwise, to assume an NSE state is achieved. Shells processed by the detonation front are not

assumed to achieve NSE anyway if their density is smaller than  $\rho_{\text{NSE0}}$ , irrespective of how high is their temperature. Instead their chemical evolution is followed with the nuclear network all the way. In practice, detonated shells are treated through the NSE routine only in a very limited set of models, because either the deflagration-to-detonation transition density of Chandra models stays below  $\rho_{\text{NSE0}}$ , or the whole subCh initial models stay below the same density, even at the center of the WD (see Table 1).

Shells that have been incinerated to NSE are assumed to stay in the statistical equilibrium state (and their chemical composition in NSE is recalculated at each time step with the new  $\rho$ ,  $T$ , and  $Y_e$ ) when their temperature is larger than  $T \geq T_{\text{out1}} = 5 \times 10^9 \text{ K}$  if density is  $\rho \geq \rho_{\text{out1}} = 5 \times 10^6 \text{ g cm}^{-3}$ , or  $T \geq T_{\text{out2}} = 5.8 \times 10^9 \text{ K}$  if density is  $\rho \geq \rho_{\text{out2}} = 10^6 \text{ g cm}^{-3}$ . Otherwise, i.e. for smaller temperatures, their abundances are fed to the nuclear network and their chemical evolution is followed solving the nuclear kinetic equations.

In thermonuclear supernova explosions, matter is neutronized by electron captures in the NSE state at high densities. In our code, the electron captures in NSE are calculated at each time step according to the NSE composition and the weak interaction rates on each nuclei. The same method is applied to obtain the neutrino cooling due to weak interactions in NSE.

Since we do not rely on tabulated neutronization rates, our code is well suited to rate the precision of the available tables of electron captures in NSE or, more precisely, how they impact on the results of the explosion. As an example, we have recomputed the hydrodynamics and nucleosynthesis of model ddt2p4\_Z9e-3.std by using the extensive NSE tables provided by [Seitenzahl et al. \(2009, hereafter S09\)](#), and show the results in the last row of Table B1. The kinetic energy and the yield of  $^{56}\text{Ni}$  we obtain match nicely those calculated without the weak table, i.e. following our standard procedure of computing the NSE composition, weak rates, and neutrino emission coupled to the hydrodynamic solver. The discrepancy in kinetic energy is of order 0.07%, comparable to our precision with respect to the parameters  $Y_{\text{thresh}}$  and  $R_{\text{thresh}}$ , while the ejected mass of  $^{56}\text{Ni}$  is only 0.7% smaller than our standard value. On the other hand, the nucleosynthesis changes drastically with respect to our standard model. Within the most abundant nuclides, which we define as those with ejected mass  $M_i > 10^{-3} M_{\odot}$  for the present purposes, we find discrepancies up to 65%, among them the important SN Ia product  $^{54}\text{Cr}$ . The yields of other neutronized nuclides such as  $^{58}\text{Fe}$  and  $^{62}\text{Ni}$  disagree from our standard model also by more than 10%. In the second row, that of nuclides whose yield is in the range  $10^{-3} M_{\odot} \geq M_i > 10^{-6} M_{\odot}$ , the largest discrepancy belongs to  $^{64}\text{Ni}$ , whose yield differs from our standard model by as much as 480%, while the discrepancy of the yield of  $^{50}\text{Ti}$  is also above 100%. Finally, within the nuclides with  $M_i > 10^{-12} M_{\odot}$ , the largest discrepancy amounts to 5020%, which is the case for  $^{48}\text{Ca}$ . We have checked that our neutronization rate and neutrino emission rate match those given in S09 at the tabulated values of  $T$ ,  $\rho$ , and  $Y_e$ , so the different nucleosynthetic results we obtain are attributable uniquely to the interpolation between the nodes of their NSE tables.

This paper has been typeset from a  $\text{\LaTeX}$  file prepared by the author.

**Table B1.** Convergence of nucleosynthesis calculations. The figures belong to model model ddt2p4\_Z9e-3\_std.

	range of yield masses ( $M_{\odot}$ )	33% of nuclides better than	67% of nuclides better than	100% of nuclides better than
$Y_{\text{thresh}} = 10^{-20} \text{ mol g}^{-1}$	$M_i \geq 10^{-3}$	0.001%	0.001%	0.07%
vs.	$10^{-3} > M_i \geq 10^{-6}$	0.001%	0.06%	2.7%
$Y_{\text{thresh}} = 10^{-19} \text{ mol g}^{-1}$	$10^{-6} > M_i \geq 10^{-12}$	0.001%	0.04%	2.2%
$R_{\text{thresh}} = 10^{-14} \text{ mol g}^{-1}$	$M_i \geq 10^{-3}$	0.001%	0.02%	0.25%
vs.	$10^{-3} > M_i \geq 10^{-6}$	0.06%	0.15%	3.3%
$R_{\text{thresh}} = 10^{-13} \text{ mol g}^{-1}$	$10^{-6} > M_i \geq 10^{-12}$	0.6%	3.6%	28%
weak rates table in S09	$M_i \geq 10^{-3}$	0.4%	2.5%	65%
vs.	$10^{-3} > M_i \geq 10^{-6}$	0.5%	1.9%	480%
our standard procedure	$10^{-6} > M_i \geq 10^{-12}$	0.4%	2.2%	5020%